Title

Impacts of Dust Non-Sphericity and Emitted Size Distribution on Saharan Dust Transport and Radiative Effects

Author

Lin, Zhuo Xuan

Publication Date

2021

Peer reviewed|Thesis/dissertation

Impacts of Dust Non-Sphericity and Emitted Size Distribution on Saharan Dust Transport and Radiative Effects

By

ZHUO XUAN LIN
THESIS

Submitted in partial satisfaction of the requirements for the degree of

MASTER OF SCIENCE

in

Atmospheric Science

in the

OFFICE OF GRADUATE STUDIES

of the

UNIVERSITY OF CALIFORNIA

DAVIS

Approved:

Shu-Hua Chen, Chair

Terrence R. Nathan

Paul Ullrich

Committee in Charge

2021

Abstract

Dust aerosols have several impacts on the Earth system, including their influence on weather and climate through their interactions with clouds and radiation. Yet, dust modeling has long been a challenge in the research and operational communities. In particular, many weather and climate models underestimate dust long-range transport and dust-radiative effect. In this study, we aim to improve modeled dust representation over the Sahara Desert and the eastern Atlantic Ocean by integrating non-spherical (tri-axial ellipsoidal) dust particle shape and globally- and locally-representative observationally-constrained dust emitted size distributions into our dust model—the Weather Research and Forecasting model coupled with an online dust module (WRF-Dust). Based on these model modifications, we conducted two sets of numerical experiments over North Africa in 2016. Our numerical experiments on dust particle shape reveal that accounting for dust non-sphericity augments overall modeled aerosol optical depth (AOD) and promotes the westward extension of low Angstrom exponent (AE) values, thanks to the reduced dust sedimentation and enhanced dust optical properties under non-spherical conditions. As AE is inversely related to the average particle size, the non-spherical dust simulated results suggest that a greater fraction of large particles is transported from the Saharan source regions into the Atlantic Ocean, but the amount still falls short. Model evaluation against the AErosol RObotic NETwork (AERONET) observations shows that in the non-spherical shape simulation, there are 7.80% and 1.30% improvements in the root mean square error (RMSE) for AE and AOD, respectively, and 15.30% and 10.21% improvements in the mean bias for AE and AOD, respectively. By constraining dust emitted size distribution, we have further improved the magnitude and spatial distribution of AOD and AE, as indicated by the reduced error against a series of satellite and ground-based observations. Moreover, in a case study of Hurricane Earl (2010), by applying the best model configuration (i.e., the setting with the best overall model performance), we have slightly improved the storm intensity in minimum sea level pressure and maximum 10-m winds, although the improvements are not significant, requiring further adjustments in modeled dust. This study demonstrates the importance of emitted dust size distribution and particle shape in accurate dust simulation, which has

far-reaching implications in numerous weather systems, such as Atlantic hurricanes, convective storms, African easterly waves (AEWs) and the African easterly jet (AEJ).

1. Introduction

Dust is one of the most abundant aerosols in the world (Prospero et al., 2002). Originating from arid desert regions including North Africa, the Middle East, Southwest Asia, and Northeast Asia, dust spreads over vast areas on its way propagating downwind, reaching the adjacent oceans and even continents across the seas under favorable conditions. With its widespread presence, dust has many impacts on the Earth system, including 1) its influence on weather and climate and Earth's energy budget through its interactions with radiation and clouds (DeMott et al., 2003; Fan et al., 2016; Pérez et al., 2006; Shi et al., 2014; Slingo et al., 2006; Tegen, 2003), 2) its effects on ecosystems through dust-related physical and biogeochemical processes (Jickells et al., 2005; R. Wang et al., 2015; Yu et al., 2015), and 3) the growing public concern about human health affected by degraded air quality and decreased agricultural productivity caused by dust storm events (Arnalds et al., 2001; Burnett et al., 2014; García-Pando et al., 2014; Morman & Plumlee, 2013; Pandolfi et al., 2014). Evaluating these dust impacts and addressing dust-induced issues call for accurate dust modeling.

Of the various dust impacts mentioned, dust impact on weather systems, in particular, via dust-radiation interaction, is of our primary interest in this study. Over North Africa, dust lifted in the air largely travels with the Saharan air layer (SAL) under the westward-propagating African easterly waves (AEWs) and the African easterly jet (AEJ) (Bercos-Hickey et al., 2020; Knippertz & Todd, 2010; Nathan et al., 2019). During the transport, dust interacts with both shortwave and longwave radiation, affecting the radiative balance over the SAL region and impacting weather systems and large-scale circulation locally and beyond the region. Specifically, incoming shortwave radiation is effectively absorbed by dust, which enhances heating around the upper dust layer. By contrast, dust extinction of shortwave radiation generates a cooling effect in the lower dust layer. Additionally, dust absorbs and scatters longwave radiation as well as emits energy in all directions, resulting in cooling in the upper dust layer and warming in the lower dust layer (Carlson & Benjamin, 1980; S.-H. Chen et al., 2010; Wong et al., 2009; Zhu et al., 2007). Studies have shown that there is a net heating effect when considering dust interaction with both shortwave and longwave radiation (Carlson & Benjamin, 1980; Wong et al., 2009; Zhu et al., 2007). It is clear that dust-radiation

interaction alters the vertical temperature profile and modifies atmospheric stability (S.-H. Chen et al., 2010), which would have an influence on weather systems in the region. Moreover, the modulated meridional temperature gradient, as a result of dust-radiative forcing, may alter the vertical wind shear and subsequently affect the intensity and direction of the AEJ (S.-H. Chen et al., 2010; Konare et al., 2008), as well as AEWs (Ma et al., 2012; Nathan et al., 2017; Nathan et al., 2019). Through its interactions with radiation and clouds, dust has a considerable influence on other weather systems, such as mesoscale convective systems (MCSs). Min et al. (2009) shows that dust acting as cloud condensation nuclei (CCN) and ice nuclei (IN) would increase cloud droplet number concentration, which would suppress precipitation. In a study of an MCS event over West Africa in August 2006, Shi et al. (2014) discovered that the dust aerosol direct effect dominated, which delayed the onset of the MCS. Despite the delayed development, the system could become more intense with more extensive anvil clouds due to the dust-radiative effect, as shown in a case study of an MCS that occurred on 4-6 July 2010 over North Africa (C.-C. Huang et al., 2019). The dust impacts discussed here again signify the importance of accurate dust representation in weather and climate models. Thus, reasonably representing dust effects in numerical models is important to weather and dust simulations.

Accurate dust modeling, however, has remained a challenge in the research and operational communities. Through extensive comparisons with in situ and remote sensing observations as well as field campaign data, dust models have exhibited some major deficiencies, such as the underestimation of aerosol optical depth (AOD). Model deficiency in AOD simulation is complicated by the fact that models often produce AOD simulations that are different not only from observations, but also among models (e.g., Li et al., 2016; Penner et al., 2001), in particular over dust aerosol dominant regions. The failure of models to capture these important dust features ultimately results in a less realistic representation of dust and thus the dust optical effects.

Other major model deficiencies include the underestimation of coarse dust amount and insufficient long-range dust transport. Coarse dust particles, however, are widely present in the atmosphere and play a key role in the dust-radiative effect. Using the Fennec field campaign data (over the Sahara) and the AER-

D field campaign data (over the tropical eastern Atlantic), Ryder et al. (2019) found that coarse (diameter > 2.5 μm) and giant (diameter > 20 μm) dust particles comprise a considerable fraction of dust mass—over the Sahara, 93% of dust mass is constituted by particles over 5 μm and 40% by particles over 20 μm; over the SAL, 61% to 89% by particles over 5 μm and 2% to 12 % by particles over 20 μm. Failing to include giant dust particles in models may lead to underestimation of shortwave and longwave extinction by 18% and 26%, respectively. Yet, many model simulations [e.g. Weather Research and Forecasting model coupled with Chemistry (WRF-Chem), Community Earth System Model (CESM), Goddard Earth Observing System coupled with Chemistry (GEOS-Chem)] show substantial negative biases (0.5-1.5 orders of magnitude underestimation, increasing with dust diameter) in coarse dust load when compared to global measurements (Adebiyi & Kok, 2020). Ansmann et al. (2017) conducted an in-depth comparison study on regional and global dust models versus shipborne (polarization/Raman) lidar observations taken over the tropical Atlantic during April-May 2013. The comparisons in simulated and observed dust profiles indicated that modeled dust was removed too efficiently by dry and wet deposition during long-range transport (~1500-5000+ km from Saharan source regions). In addition, the modeled fine-to-coarse ratio was too high, suggesting that the models overestimated fine dust particles. They further found that the deviation of the modeled ratio was increasingly high with long-range transport.

To cope with the model deficiencies in AOD and coarse dust representation, Kok et al. (2017) utilized an array of observational, modeling, and experimental constraints on dust properties, including the global dust AOD, averaged dust extinction efficiency, averaged emitted dust size distribution, and averaged size-resolved dust lifetime. Similarly, Adebiyi & Kok (2020) employed globally representative constraints on dust properties. Instead of combining constraints on the emitted dust size distribution and dust lifetime, they directly used published in situ measurements of dust size distributions, resulting in a greater contribution by coarse dust compared to Kok et al. (2017) [see Fig. 1 in Adebiyi & Kok (2020)]. Nevertheless, the constrained distributions in both studies have substantially increased coarse dust concentration.

Dust shape is another key, yet often overlooked, factor that is significant to the model characterization of dust. Real-life dust particles are irregular in shape, anisotropic, and inhomogeneous (Nousiainen, 2009). Yet, a common practice in early and some current models is to treat dust particles to be spherical, thus allowing the use of Mie theory in computing the single-scattering properties of dust particles (Nousiainen, 2009). Although dust sphericity is a reasonable assumption to some extent (Koepke et al., 2015), studies have shown that the simplified assumption of spherical dust particles may introduce considerable errors in dust modeling (e.g., Dubovik et al., 2002; Ginoux, 2003; Kok et al., 2017; Nousiainen, 2009). Compared to non-spherical particles, spherical particles at the same volume and mass are subject to faster gravitational settling because they experience less aerodynamic drag (Yang et al., 2013). Early sedimentation of dust particles in model simulations (e.g., Ansmann et al., 2017; O'Sullivan et al., 2020), in combination of the absence of coarse dust particles in models, further contributes to the underestimation of dust. Another drawback arising from the spherical assumption is the decreased dust optical properties, manifested as the underestimation of AOD when compared to observation data (Hoshyaripour et al., 2019). Without considering dust non-sphericity, models could underestimate AOD as much as 30% (Potenza et al., 2016), possibly owing to the greater surface-to-volume ratio of non-spherical dust particles than that of volume-equivalent particles (Kalashnikova & Sokolik, 2004).

Numerous studies (e.g., Bi et al., 2009; Dubovik et al., 2006; Meng et al., 2010; Mishchenko et al., 1997; Nousiainen, 2009) have been dedicated to developing a non-spherical (e.g., spheroidal, ellipsoidal, etc.) particle shape model that best captures properties of real dust. Bi et al. (2010) discovered that the tri-axial ellipsoidal shape model showed better agreement with experimental measurements than the spheroidal model, especially in terms of the polarization characteristics. By adopting the tri-axial ellipsoidal model, Y. Huang et al. (2020) found that sedimentation of dust particles slows down by ~15% due to greater drag force.

This study builds on the invaluable findings and understanding from previous studies. We will incorporate appropriate adjustments to our dust model in the aspects of emitted dust size distribution and dust particle shape in order to improve dust representation (discussed in detail in Section 2), which will

facilitate our investigation of dust impacts on weather systems. Our regions of interest are the Sahara Desert in North Africa, which is the largest source of dust aerosols in the world (Prospero et al., 2002), and the eastern Atlantic Ocean. The Sahara Desert has annual dust emissions of 200-3,000 Tg (Huneeus et al., 2011), which constitute about 25% of the global AOD (Kinne et al., 2006). To improve dust modeling, this study incorporates observationally-constrained dust size distribution based on Adebiyi & Kok (2020) and adopts a more realistic dust shape in the model.

The paper is organized as follows: Section 2 discusses the details of the model and model modifications; Section 3 describes the ground-based and satellite observation data used for model evaluation; Section 4 delineates the experimental design based on each model modification, followed by the model results and evaluation against the observations; in Section 5, we apply the best model configuration from Section 4 to investigate the effect of improved dust simulation on model meteorological fields through a case study on Hurricane Earl (2010); finally, Section 6 summarizes our findings and explores future work that will further improve the robustness of the dust model.

2. Numerical model and model improvements

2.1. Model description

In this study, we use the Weather Research and Forecasting (WRF) model V3.7.1 (Skamarock et al., 2008) coupled with an online dust module (WRF-Dust) developed by S.-H. Chen et al. (2010, 2015) to conduct our numerical simulations. We will briefly describe the dust model here. Further details can be found in the original published papers. The WRF-Dust model incorporates a dust continuity equation that accounts for dust transport, mixing due to subgrid boundary layer turbulence, dust sedimentation, and source and sink processes. The source and sink term represents multiple dust processes, including surface dust emissions, dry and wet deposition, and other dust-microphysical processes (e.g., dust activated as CCN and/or IN, dust scavenged by clouds). Surface dust emissions, in particular, occur only when the following conditions are met: the vegetation type is barren; the volumetric soil moisture is less than 0.2; and the 10-m wind speed (u_{10}) exceeds a threshold wind speed (u_{10c}) of 6 m s^{-1}. The surface vertical dust flux (F_d) is

calculated as: $F_d = C(u_{10} - u_{10c})u^2_{10}$, where C is the dimensional constant set to 0.4 μg m^2 s^{-5}, following Tegen & Fung (1994).

The model uses five size bins, with median dust radii of 0.25, 0.5, 1, 2, and 4 μm, and the two largest bins (2 and 4 μm) are considered as coarse or large particles following Ryder et al. (2019). The dust bin size distribution and dust emission flux weighting for each size bin are constructed upon the scale-invariant theoretical analysis in Kok (2011), which describes that the emitted dust size distribution is independent of meteorological conditions (e.g., wind speed) and soil characteristics (e.g., soil moisture and soil type). The model uses the Optical Properties of Aerosols and Cloud (OPAC) software package (Hess et al., 1998) to compute the dust optical properties, including the single-scattering albedo, asymmetry factor, and extinction coefficient, at different wavelengths, including both shortwave and longwave.

The WRF-Dust model configurations thus far align with those in S.-H. Chen et al. (2015). During model testing, however, we discovered an issue that the background CCN and IN aerosol concentrations in the two-moment microphysics scheme (Cheng et. al., 2010) used in the WRF-Dust model would diminish over time because there is no recharge of background aerosols from lateral and lower boundaries of the domain after the consumption by CCN activation and IN nucleation. As a result, in this version of WRF-Dust, we have constrained lateral boundary values of CCN and IN aerosol concentrations to their initial values (i.e., zero tendency) at the inflow regions (i.e., an open boundary condition) and replenished the background concentrations back to their initial values inside the domain (G. Chen et al., 2015). The replenishment is performed using the Newtonian relaxation method (Stauffer & Seaman, 1990) with 2-day relaxation time.

2.2. WRF-Dust model improvements

In this section, we will introduce two major modifications on dust shape and emitted dust size distribution to improve the WRF-Dust model simulations. The first modification adopts a tri-axial ellipsoidal dust model to more accurately represent real dust. Accounting for dust non-sphericity may lead to decreased dust sedimentation (increased dust lifetime) and enhanced dust optical properties. The second modification integrates observationally constrained size distributions into the model dust emissions scheme,

which helps to improve emitted dust particle size representation in the model. The details of each major modification and the implementation strategies are discussed in the following subsections.

2.2.1. Non-spherical dust shape

To consider the dust shape effect, we assume a tri-axial ellipsoidal dust particle shape. Although this assumption is quite idealized, it allows a better representation of real-life dust (Y. Huang et al., 2020). The tri-axial ellipsoid model involves two distinctive shape descriptors: the aspect ratio (AR) and the height-to-width ratio (HWR). The AR is defined as the ratio of the longest dimension of an ellipsoidal dust particle's horizontal cross-section (i.e., the major axis of the projected ellipse, L) to its perpendicular dimension (i.e., the minor axis, W). The HWR, as its name suggests, is a ratio accounting for the particle's height (H) and W, where H is the dimension perpendicular to the collection plane surface (Fig. 1). The AR and HWR are included in the calculation of the dust particle shape factor ($\chi = v_{sph}/v_{asp}$; where v_{sph} and v_{asp} are the terminal velocities of a spherical particle and a non-spherical particle, respectively), which can be used to characterize particle sphericity. χ is unity for spherical particles and greater than 1 for non-spherical particles. To estimate χ, we apply Equation (25) from Bagheri & Bonadonna (2016) that accounts for the three dimensions of a tri-axial ellipsoid:

$$\frac{v_{sph}}{v_{asp}} \equiv k_s = \frac{1}{2}\left(F_s^{1/3} + \frac{1}{F_s^{1/3}}\right) \quad (1)$$

where k_s is equivalent to our shape factor (χ) and F_s is the Stokes form factor that can be obtained from $\mathrm{HWR}\cdot(1/\mathrm{AR})^{1.3}$. The factor χ can then be used to modulate the dust terminal velocity caused by the non-spherical shape, and the terminal velocity equation is now written as:

$$v = \frac{1}{18}\frac{D^2 \rho_p g}{\chi \mu} \quad (2)$$

where D is the diameter of a spherical particle or the volume-equivalent diameter of a non-spherical particle, $\rho_p = 2.5 \times 10^3$ kg m^{-3} is the typical dust density (Kok et al., 2017), g is the gravitational acceleration at the Earth's surface, and $\mu = 1.8 \times 10^{-5}$ kg m^{-1} s^{-1} is the air viscosity in a standard atmosphere (temperature at

298 K and pressure at 1 atm). The terminal velocity of non-spherical particles decreases compared to the volume-equivalent spherical particles, as $\chi > 1$ for non-spherical particles. This will allow non-spherical dust particles to be suspended in the air longer. Y. Huang et al. (2020) shows that considering a tri-axial ellipsoidal dust shape reduces the gravitational settling speed by ~15% and enhances the dust gravitational settling lifetime by ~20% on a global average.

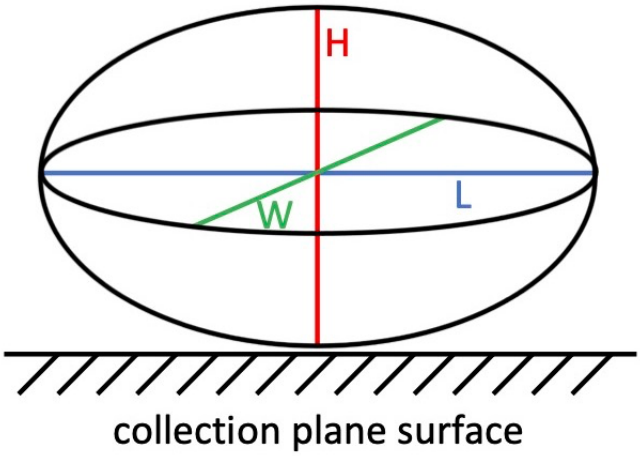

Fig. 1. *A schematic diagram of an irregularly shaped dust particle represented by a tri-axial ellipsoid. The length L (blue line), or the major axis, is the longest dimension of the top-down projection of the ellipsoid. The width W (green line), or the minor axis, measures the maximum distance across the particle that is perpendicular to L. The height H (red line) records the maximum particle distance perpendicular to the collection plane surface, which is also perpendicular to L and W.*

For this study, we use measurements of AR and HWR of African dust from multiple studies and field campaigns (C. Chou et al., 2008; Kandler et al., 2007; Klaver et al., 2011; Lieke et al., 2011; Reid et al., 2003). With these measurements, we can obtain the averaged shape factor for each size bin diameter (1.291, 1.291, 1.286, 1.284, and 1.295 for bins 1-5, respectively). The shape factors are then incorporated into the model calculation of terminal velocity, allowing the model to considerably reduce the speed of dust sedimentation, in agreement with the conclusion in Y. Huang et al. (2020).

In addition to slowing down dust sedimentation, dust non-sphericity has a positive impact on the dust optical properties and AOD due to the change of the particle cross section. A non-spherical particle, on average, has a greater surface-to-volume ratio compared to a volume-equivalent spherical particle

(Hoshyaripour et al., 2019). A closely related concept is the cross section, or projected area. For a randomly oriented dust particle, its projected area is approximately ¼ of the surface area (M. Wang et al., 2019). Due to the enlarged particle cross section, non-spherical dust particles undergo enhanced dust-radiation interactions (i.e., extinction), which, in turn, may increase dust AOD. We can see this enhancement due to the enlarged area from the following modified optical depth equation:

$$\tau_c(\lambda) = h \sum_i^n \sum_j^m Q_{ei,j}\left(\lambda, D_{ei,j}\right) \gamma A_{ci,j} N_{i,j} \quad (3)$$

The equation represents the optical thickness (τ_c) of N (# m^{-3}) particles in relation to the extinction efficiency (Q_e), which is a function of wavelength and the dust effective diameter (D_e), and cross section area (A_c). γ is the non-spherical area factor that accounts for the increased cross section area of non-spherical particles; thus, $\gamma > 1$ for non-spherical particles. The subscripts i and j denote the aerosol type and the size bin, respectively; n is the number of total aerosol types, which is 1 since only dust aerosol is considered in the WRF-Dust model; and m is the number of total size bins, which is 5 in this study. Equation (3) shows that a particle's optical thickness is proportional to its cross section area, from which we can infer that non-spherical dust particles enhance the overall model AOD. The computation results of the non-spherical area from the shape factors obtained earlier indicate an average of 4.4% increase in cross section area of a non-spherical dust particle relative a spherical one. Subsequently, we implement the non-spherical modifications of dust optical properties into the Goddard Space Flight Center (GSFC) radiation scheme (M.-D. Chou & Suarez, 1994, 1999; M.-D. Chou et al., 2001). Note that in the GSFC scheme, the five model size bins are lumped into three modes (nucleation, accumulation, and coagulation modes) in the computation of optical properties.

Besides integrating the dust non-sphericity impact into the optical thickness equation, we have devised an approach that allows us to directly modify the dust optical properties so that dust non-sphericity is considered. The calculations of non-spherical dust optical properties are based on the OPAC refractive index data and the database software package developed by Meng et. al (2010), which computes the single-scattering properties of dust-like aerosols using a combination of the Lorenz-Mie theory, the T-matrix

method, the discrete dipole approximation, and an improved geometric optics method. The computed values for a total of 18 bands [6 shortwave and 12 longwave bands, based on the Fu-Liou-Gu (FLG) radiation scheme (Fu & Liou, 1992; Gu et al., 2011)] at different bin diameters are stored in lookup tables to replace the spherical optical properties. This method to obtain non-spherical optical properties is necessary for simulations using the FLG radiation scheme because using the original optical coefficients in the WRF-Dust model with the FLG scheme would generate consistently negative Angstrom exponents (AE; discussed in further details in Section 3.1), which is problematic as it neither represents the real dust behavior nor reflects true model performance. The issue is related to AOD at the shortwave bands and pending further investigation. Unfortunately, the updated lookup tables, which are bandwidth-dependent, are only available for the FLG scheme at present. Lookup tables for other radiation schemes, such as the GSFC radiation scheme, will be implemented in the future.

2.2.2. Emitted dust size distribution

We improve the model emitted dust size distribution through constraints with global observations developed by Adebiyi & Kok (2020) and Adebiyi et al. (2020). As discussed in the introduction, the constraints are based on published in situ measurements of atmospheric dust size distributions globally, observational and experimental constraints on dust shape and optical depth, and an ensemble of global model simulations [i.e., DustCOMM, or Dust Constraints from joint Observational-Modelling-experiMental analysis, developed by Adebiyi et al. (2020)]. These constraints are parameterized and used in the generalized atmospheric dust size distribution equation (Adebiyi et al., 2020):

$$\frac{dV_{atm}(D)}{dD} = \frac{1}{C_V^*} \cdot \left[1 + erf\left(\frac{\ln\left(\frac{D}{D_s}\right)}{\sqrt{2}\ln(\sigma_s)} \right) \cdot e^{\left[-\left(\frac{D}{\Lambda}\right)^{\alpha}\right]} \cdot D^b \right] \quad (4)$$

where D is the dust geometric diameter, $dV_{atm}(D)/dD$ is the volume size distribution of atmospheric dust, C_V^* is the normalization constant, *erf* is the error function, D_s (geometric median diameter) and σ_s (geometric standard deviation) are least-squares fitting parameters, and α, b, and Λ are adjustable parameters pertaining

to coarse dust particles. The parameters for the globally-averaged observationally-constrained (hereafter GLO) dust size distribution used in the model can be found in Table 1. Compared to the emitted dust size distributions in other global simulations (e.g., WRF-Chem, CESM, etc.), the GLO distribution is shown to substantially increase the model coarse dust loading, bringing the dust size distribution much closer to the observed distribution [see Fig. 1 in Adebiyi & Kok (2020)].

In addition to the GLO size distribution, similarly, we develop an observational constraint focusing on North Africa, our region of interest. The locally representative observationally-constrained (hereafter LOC) dust size distribution is an averaged size distribution based on measurements at five AErosol RObotic NETwork (AERONET) sites over 13-17°N—Cape Verde (CV; 16.733°N, 22.935°W), Dakar (DA; 14.394°N, 16.959°W), IER_Cinzana (IC; 13.278°N, 5.934°W), Banizoumbou (BA; 13.547°N, 2.665°E), and Zinder Airport (ZA; 13.777°N, 8.990°E)—along which major dust plumes propagate (see Fig. 2 for AERONET site locations). The choice of AERONET sites will be discussed in detail in Section 3.1. Size distribution parameters specific to the above-mentioned locations are presented in Table 1. Compared to the GLO distribution, LOC shows even more dust loading toward the coarse end of the distribution (10-20 μm diameters) but less amount otherwise (Fig. 3).

Table 1. *Values of the observationally-constrained emitted size distribution parameters for the globally-averaged dust size distribution and five local dust size distributions at CV, DA, IC, BA, and ZA.*

Distribution Type	Location	D_s (μm)	σ_s	α	b	Λ
GLO	Globe	2.50	2.07	0.02	-1.08	23.54
LOC	Cape Verde	1.37	1.83	2.42	-0.20	15.40
	Dakar	1.64	1.86	0.21	-0.41	346.35
	IER_Cinzana	1.17	1.77	0.03	-0.12	281.03
	Banizoumbou	0.97	1.74	0.58	0.19	32.96
	Zinder Airport	0.80	1.68	0.07	0.34	8.73

To integrate the observationally constrained emitted dust size distributions into the model, we partition each distribution into five segments according to the five size bins of the model, with each bin diameter being the median diameter of each distribution segment. The weighting of each segment is then computed based on Equation (4) and incorporated into the model as the dust emission flux weighting or ratio for the

corresponding size bin. Note that the model size bins are capped at 8 μm in diameter. Thus, we have incorporated the constrained distributions only up to 10 μm in dust geometric diameter (with 8 μm being the median diameter in the last distribution segment). The computed size bin weightings are recorded in Table 2. Compared to ORG, GLO puts greater emphasis on bins 1-4, whereas LOC favors bins 1, 3, and 4 more strongly. Due to the model limitation in dust particle size, the contribution of the largest particles in the distribution (diameters of 10-20 μm) is neglected, which may affect the coarse dust representation in model simulation. In the future, we will extend the model size bins to 20 μm so that we can fully apply the distributions into our WRF-Dust model.

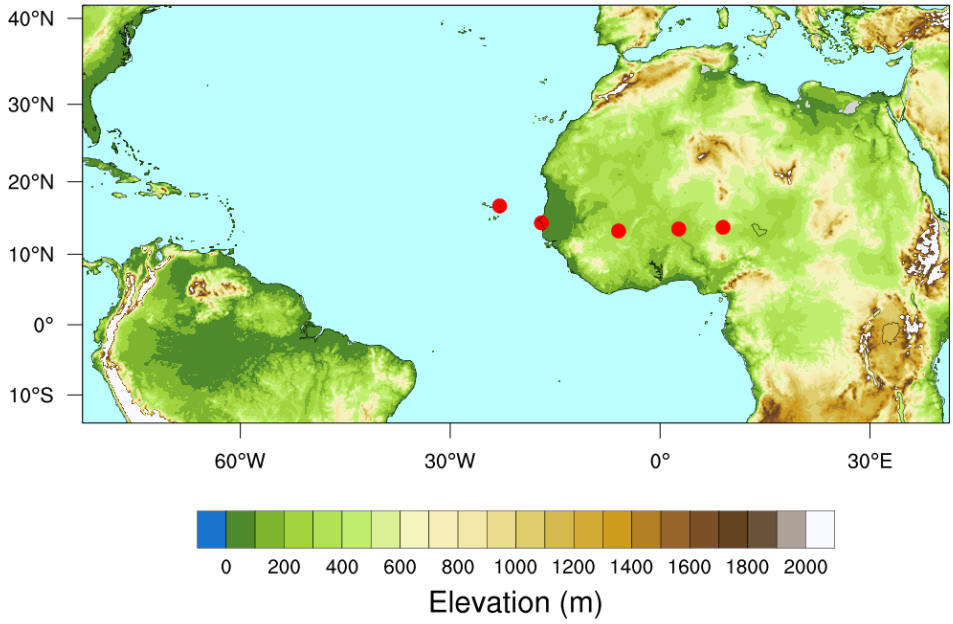

Fig. 2. *AERONET sites examined in this study (denoted by red dots). From west to east, the sites are Cape Verde (CV), Dakar (DA), IER_Cinzana (IC), Banizoumbou (BA), and Zinder Airport (ZA). Note that the figure also displays the domain configuration of our dust numerical experiments.*

Table 2. *Dust emission flux weighting of each model size bin (median radius in parentheses) calculated based on different emitted dust distributions. The sum of the five bins' weightings is equal to 1.*

Distribution Type	**Weighting by Bin**				
	Bin 1 (0.25 μm)	**Bin 2 (0.5 μm)**	**Bin 3 (1 μm)**	**Bin 4 (2 μm)**	**Bin 5 (4 μm)**
ORG	0.007	0.053	0.09	0.25	0.60
GLO	0.013	0.072	0.218	0.375	0.322
LOC	0.016	0.047	0.093	0.372	0.472

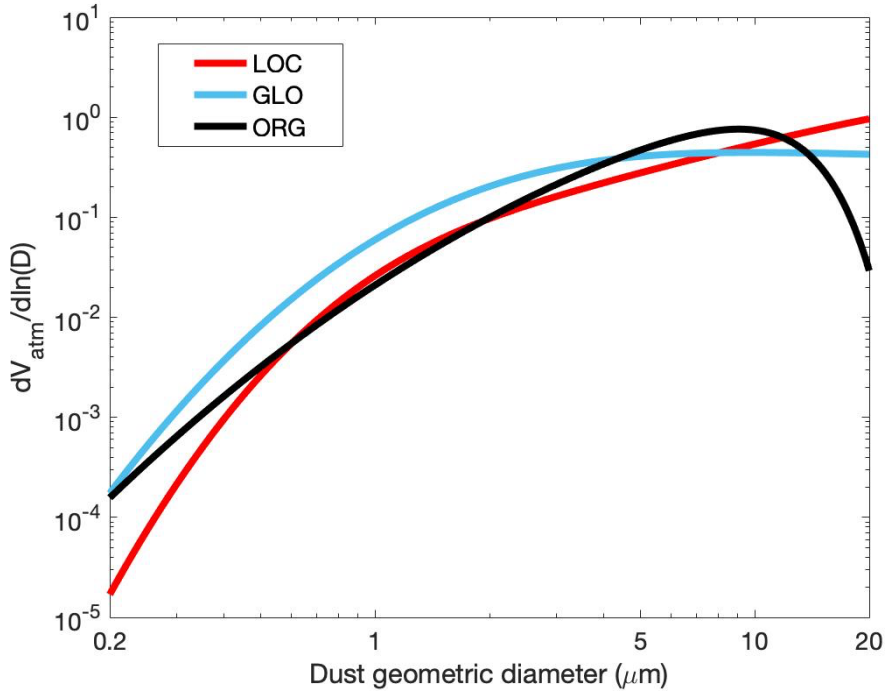

Fig. 3. *Three normalized emitted dust size distributions used in the study: LOC (red), GLO (blue), and ORG (black). LOC and GLO represent the locally-averaged (over the five AERONET sites in Table 1) and globally-averaged observationally-constrained distributions, respectively, whereas ORG represents the distribution originally used in the WRF-Dust (S.-H. Chen et al., 2015), which is based on Kok (2011).*

3. Observations

Observations will be used to verify model results in the aspects of AOD magnitude and pattern, AOD-derived parameter (i.e., AE), and vertical aerosol backscatter profiles. The observation data used are from various ground-based and satellite remote sensing data, including AOD and AE from AERONET, AOD and AE from the Visible Infrared Imaging Radiometer Suite (VIIRS) onboard the Suomi National Polar-Orbiting Partnership (Suomi NPP) spacecraft, aerosol backscatter profiles from the Cloud-Aerosol Lidar with Orthogonal Polarization (CALIOP) onboard the Cloud-Aerosol Lidar and Infrared Pathfinder Satellite Observation (CALIPSO) satellite, and AOD from the Moderate Resolution Imaging Spectroradiometer (MODIS) onboard the Terra and Aqua satellites. Each set of observation data and its role in model validation will be briefly introduced in the following subsections.

3.1. AERONET AOD and AE

AERONET is a network of ground-based remote sensing aerosol observation sites developed by NASA and PHOTONS (PHOtométrie pour le Traitement Opérationnel de Normalisation Satellitaire) and continuously expanded by national agencies, institutes, universities, and researchers around the world. AERONET provides aerosol observations including AOD, AOD-dependent products, such as the AE, inversion products, and precipitable water in different regimes. For model verification in this study, we use Level 2 (calibrated, cloud-screened, and quality-ensured) AOD and the derived AE data in Version 3, which utilizes the latest processing algorithms (Giles et al., 2019). AE is a parameter that describes the wavelength dependence of AOD and is often used as an indicator of the average particle size. The Angstrom's empirical expression (Ångström, 1929) is: $\tau(\lambda) = \beta\lambda^{-\alpha}$, where λ is the wavelength, $\tau(\lambda)$ is the wavelength-dependent AOD, β is the Angstrom's turbidity coefficient, and α is the AE. Given two different wavelengths, we may obtain the AE as:

$$\alpha = -\frac{d\ln\tau}{d\ln\lambda} = -\frac{\ln\left(\frac{\tau_1}{\tau_2}\right)}{\ln\left(\frac{\lambda_1}{\lambda_2}\right)} \quad (5)$$

where the subscripts 1 and 2 represent two distinct wavelengths. AE is inversely related to the mean particle size. Generally, $\alpha \leq 1$ indicates coarse-mode dominant aerosols, while $\alpha \geq 1$ indicates fine-mode dominant particles (Soni et al., 2011).

We have chosen, as mentioned in Section 2.2.2, five AERONET sites in the region of interest for model verification (Fig. 2), including CV, DA, IC, BA, and ZA. These five sites are spread and largely aligned in the east-west direction, along which major dust plumes propagate from the inland Bodélé Depression to coastal West Africa following the prevailing AEJ. This enables us to analyze the model performance in transporting dust (via AOD comparison) and sustaining coarse dust in the air during transport (via AE comparison).

3.2. VIIRS AOD and AE

VIIRS is one of the key instruments onboard the Suomi NPP satellite, observing the entire Earth twice a day at an elevation of 824 km above sea level. VIIRS has 22 imaging and radiometric bands, allowing it to generate high-resolution visible and infrared imagery and gather global observations that facilitate environmental monitoring and numerical forecasting. AOD and AOD-derived AE use visible and near-infrared channels in solar radiation, thus they are only available once a day. For our model verification, we compare experiment results with the VIIRS Level 2 Deep Blue aerosol product (6 km × 6 km resolution), which retrieves AOD at a reference wavelength of 550 nm using two retrieval algorithms: Deep Blue algorithm over land and the Satellite Ocean Aerosol Retrieval (SOAR) algorithm over ocean (Sayer et al., 2018); and calculates AE at the visible band over land (412-488 nm over arid land, 488-670 nm over vegetated and mixed surfaces) and at both the visible and near-infrared bands over ocean (e.g., 550-865 nm). Due to limited bands associated with the model's radiation schemes in the visible spectrum—specifically, 412 and 488 nm wavelengths fall into the same band in both the GSFC and FLG radiation schemes—we will compare modeled and VIIRS-observed AE over ocean only. The satellite AOD and AE observations provide a broad picture of dust optical thickness and particle size distribution over the domain that is otherwise not fully visible through ground-based observations, such as AERONET. In addition, VIIRS Deep Blue data does not exhibit severe AOD discontinuity from ocean to land for our study period of July 2016, an issue sometimes encountered by MODIS onboard the Aqua and Terra satellites (Levy et al., 2005). Therefore, VIIRS is a suitable choice of observation for comparing with the spatial distribution and magnitude of modeled AOD (both land and ocean) and AE (ocean only), from which we can determine if the dust is reasonably distributed and if the larger particles are sustained in the air and transported sufficiently far.

3.3. CALIOP aerosol backscatter profiles

CALIOP, an important instrument onboard the CALIPSO satellite, is a two-wavelength polarization-sensitive lidar, which generates high-resolution aerosol and cloud vertical profiles (Winker et al., 2003). CALIOP measures backscatter intensity at 1064 nm and orthogonally polarized components of the

backscatter at 532 nm, and the latter is used for model evaluation. The vertical and horizontal resolutions of CALIOP are 30-60 m and 333 m, respectively. For model validation, we statistically compare the modeled and CALIOP aerosol backscatter profiles. The details of the statistical evaluation are outlined in Section 4.3.2.

3.4. MODIS AOD

MODIS onboard the Aqua and Terra satellites scans the entire Earth every 1 to 2 days. It operates in 36 spectral bands from 0.405 to 14.385 μm. MODIS provides important measurements and imaging that are essential to the understanding of large-scale global dynamics. For model validation, we utilize the MODIS Level 2 aerosol data product (6 km × 6 km resolution) to evaluate AOD at 550 nm for the Hurricane Earl case study. Due to the fact that the cyclone occurred in 2010, prior to the launch of Suomi NPP, VIIRS is not available for model evaluation. The MODIS dataset contains a merged AOD product, which combines both the Dark Target and Deep Blue algorithms. The merged product provides an effective representation of AOD over both dark and bright surfaces, which is advantageous since our study region contains both desert and nearby vegetated surfaces as well as the ocean.

4. Examination of dust shape effect and emitted dust size distribution effect on dust simulation

In this study, we carry out two sets of sensitivity numerical experiments. These numerical experiments explore the contributions of dust non-sphericity (Section 4.2) and various emitted dust size distributions (Section 4.3) towards the improvement of dust propagation and dust optical properties. The experimental configuration with the best simulation performance is then applied to conduct a case study on Hurricane Earl (2010) to examine impacts of improved dust simulation on meteorological fields in Section 5.

4.1. Sensitivity numerical experiment configuration

The WRF-Dust model is used for numerical simulations. The model configuration summarized in Table 3, including physics parameterization schemes, is used in all numerical experiments in Sections 4.2 and 4.3.

The experiments use a 12-km resolution domain ranging over 85°W-40°E and 10°S-40°N, covering Central and North Africa as well as a large portion of the Atlantic Ocean, spanning much of the tropical and North Atlantic (see Fig. 2). This domain configuration allows the model to simulate dust emissions originated from major Saharan source regions including the Bodélé Depression in Chad and parts of Mauritania, Mali, and Algeria (Engelstaedter & Washington 2007), and to capture the dust transported downwind by the AEJ and AEWs across the African continent and the Atlantic Ocean.

Table 3. *WRF-Dust model configurations used throughout the numerical experiments.*

Horizontal Resolution	12 km × 12 km
Vertical Layers	45
Initial and Boundary Conditions	ERA5 (Hersbach et al., 2020)
Microphysics	Two Moment Scheme (Cheng et al., 2010; C.-C. Huang et al., 2019)
Surface Layer Physics	Revised MM5 Scheme (Jiménez et al., 2012)
Land Surface Physics	Unified Noah Land Surface Model (Tewari et al., 2004)
PBL Physics	MRF Scheme (Hong & Pan, 1996)
Cumulus Parameterization	New Tiedtke Scheme (Zhang & Wang, 2017)

We have chosen July 2016 for the study, as the peak of dust emissions occurs during the summer (Engelstaedter & Washington, 2007; Kim et al., 2014; Laken et al., 2013); in winter and spring months, dust emissions decline and other aerosol emission sources, such as biomass burning, become important and cannot be simply ignored. To initialize the model, we use the ECMWF (European Centre for Medium-Range Weather Forecasts) Reanalysis v5 (ERA5) data (Hersbach et al., 2020) for the model's meteorological initial and boundary conditions. Each experiment runs for 1.5 months from 15 June to 31 July 2016; the first half month serves as model spin-up to produce background dust due to the absence of dust in the initial conditions, and the results of which are discarded. As the experiments focus on dust size distribution, transport, and optical properties, in order to constrain the modeled meteorological conditions to the observed, we employ the four-dimension data assimilation (FDDA) technique throughout all sensitivity experiments. Since we use hourly ERA5 reanalysis data for nudging, the model can capture diurnal cycles within the boundary layer, and thus, the FDDA is applied to the entire domain including the boundary layer.

4.2. Dust particle shape effect

4.2.1. Experimental design

We conduct two numerical experiments to investigate the impacts of dust shape on dust transport and optical properties in the model. Both experiments are carried out under the same model settings (see Table 3), with the exception that one assumes a spherical dust particle shape, serving as the control run, while the other considers a non-spherical shape. As the emitted dust size distribution and the radiation scheme are not of particular concern in this set of experiments, we use the distribution originally implemented in the WRF-Dust model by S.-H. Chen et al. (2015), which was established upon the scale-invariant dust distribution derived in Kok (2011) (this distribution setting will be referred to as ORG hereafter for simplicity), and the GSFC radiation scheme. The two experiments are ORG_SPH and ORG_NSPH (Table 4), which denote the spherical dust and non-spherical dust experiments, respectively. The experiment results will be evaluated against observation data to quantify improvement as a result of the tri-axial dust shape consideration.

Table 4. *The design of the two dust particle shape numerical experiments.*

Size Distribution/Radiation Scheme	Dust Shape	Experiment
ORG/GSFC	Spherical	**ORG_SPH**
ORG/GSFC	Non-spherical (tri-axial ellipsoidal)	**ORG_NSPH**

4.2.2. Results and discussion

Over land, the AOD and AE analysis results from the two dust shape experiments are statistically evaluated against the observations of the five interested AERONET sites. Since the AERONET observations are recorded at a higher and irregular temporal frequency during the daytime, we define a 2-hour window centered at each WRF analysis time (i.e., the time period ranging ±1 hour from the analysis time); within this window, we average the available AERONET data, and the averaged value is used for statistical comparison with model outputs, whose frequency is every 2 hours. In the span of the analysis month, a total of 402 valid pairs of model and observation data are included in the statistical computation, and the results are recorded in Table 5. In both the AE and AOD comparisons, ORG_NSPH produces

smaller root mean square errors (RMSEs; 7.80% and 1.30% improvements for AE and AOD, respectively) and mean biases (MBs; 15.30% and 10.21% improvements for AE and AOD, respectively) than does ORG_SPH. The enhanced AOD over the source regions and reduced sedimentation in ORG_NSPH lead to the overall improvement in dust simulation.

Table 5. *Statistical evaluation of model AE and AOD for the ORG_SPH and ORG_NSPH experiments against AERONET data. Statistics below are based on 402 valid comparisons of hourly model and AERONET data.*

Experiment	**AOD**		**AE**	
	RMSE	MB	RMSE	MB
ORG_SPH	0.309	-0.235	0.231	0.170
ORG_NSPH	0.305	-0.211	0.213	0.144

Figure 4 shows the monthly mean 550 nm AOD from VIIRS observations and model simulations. We focus on the results north of the equator, over which dust aerosols dominate. Of the two dust shape experiments, ORG_NSPH generates higher AOD overall than does ORG_SPH mainly due to the enhanced optical effects induced by non-spherical particles, coupled with the particles' delayed sedimentation, allowing more dust particles sustaining in the air to interact with incoming solar radiation. The augmented model AOD brings the modeled dust closer to the VIIRS observations—in particular, ORG_NSPH performs better in simulating dust in the Algeria and Chad source regions as well as off the coast of Africa. More dust is suspended in the air and transported farther to the Atlantic Ocean in ORG_NSPH, with AOD of 0.15-0.2 reaching over 50°W, as opposed to around 45°W in ORG_SPH. However, the increased AOD pattern in ORG_NSPH also causes a ~26% overestimation near coastal Mauritania at ~15°W, compared to ~13% in ORG_SPH. Overall, the AOD analysis shows a similar AOD spatial pattern across the model and observations, yet the model displays some discrepancies in AOD magnitude especially over major dust source regions (e.g., near 25°N, 0° in the Algeria-Mali region and near 20°N, 15°E in the Chad region). The dust hotspots in Mali and Algeria are often associated with the Saharan heat low (SHL) during the summer, which is a thermal low stationed over North Africa in response to heating at low levels (Lavaysse et al. 2009). The uncertainty of the SHL intensity and location in reanalysis and thus in WRF-Dust simulations (due to FDDA), due to the lack of observational data over the desert, may introduce difficulties

in dust simulation. On the other hand, the Chad source region is situated in a convective region that is prone to haboobs, or convective dust storms, during summer. The model's failure to simulate high AOD at source regions is caused in part by model resolution or potential model deficiencies, in addition to FDDA which may suppress convection. It is also worth noting that there exist uncertainty and biases for VIIRS Deep Blue AOD and AE retrievals. Sayer et al. (2018) finds that a typical uncertainty on 550 nm AOD is ±(0.03+10%). Additionally, a noticeable discontinuity in AOD at ~45°W can be seen in the VIIRS Deep Blue observations. A more rigorous comparison, which incorporates other algorithms and/or satellite products, is necessary in future model assessment.

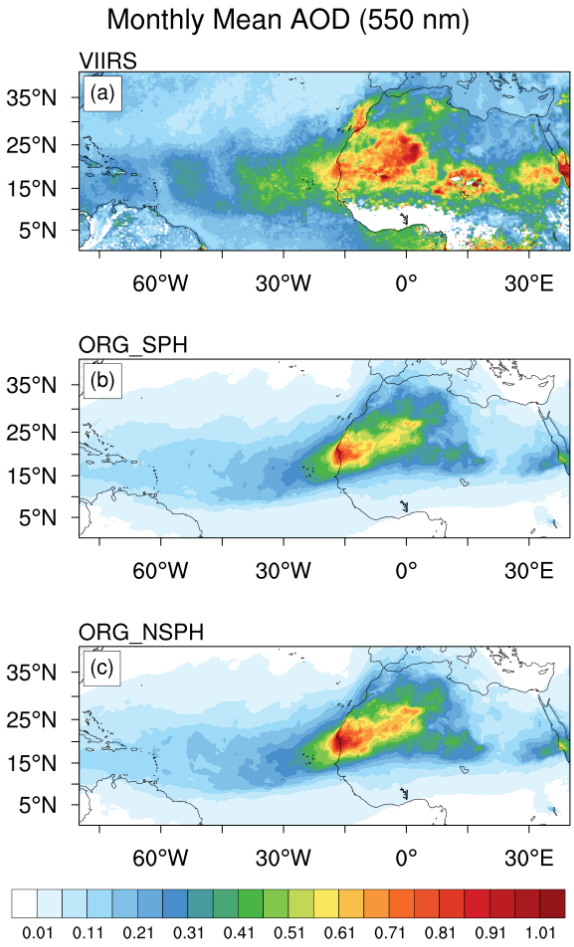

Fig. 4. *Monthly mean AOD (550 nm) over the region of interest for July 2016. (a) VIIRS Deep Blue observed AOD. (b-c) Modeled AOD for the two dust shape numerical experiments: ORG_SPH and ORG_NSPH, respectively.*

In addition to AOD evaluation, analysis on the AE pattern and magnitude may lend us some insight into the model performance in transporting dust downwind from its sources, in particular for large particles. Figure 5 depicts the monthly mean over-ocean 550-865 nm AE for VIIRS observations and the two dust shape experiments. Along the major dust plume region (~15°N), observed AE increases westward from the West African coast over the eastern side of the Atlantic, implying a greater fraction of large aerosol particles on the eastern side than on the western side of this region. However, observed AE starts decreasing past ~40°W, which suggests that there is an increasing fraction of large aerosol particles over the western Atlantic. For the model simulations, despite the two numerical experiments producing different AE magnitudes, both experiments produce AE that monotonically increases westward from the West African coast. Smaller modeled AE values toward the West African coast are expected since the area is dominated by large dust particles, while the increasing AE away from the coast represents the increasing dominance of smaller particles away from their source regions. The reduction of observed AE over the western Atlantic is because marine aerosols, another type of large aerosols, have a greater contribution to AE there than dust aerosols, which are predominantly composed of relatively small particles after long-range transport. The model is unable to reproduce this feature over the western Atlantic since marine aerosols are not included in our WRF-Dust model. As a result, we superimpose a contour line of 0.25 modeled AOD on the modeled AE plots (see Fig. 5b and c), beyond which AOD is generally lower than 0.25, indicating the waning contribution of dust and the growing dominance of marine aerosols. Thus, our model AE evaluation over the ocean mainly focuses on the area enclosed by the contour and the African coast.

Compared to ORG_SPH, not only is ORG_NSPH more effective in transporting dust westward to the ocean (i.e., higher AOD in Fig. 4c than in Fig. 4b) but also improves AE simulation (i.e., smaller AE in Fig. 5c than in Fig. 5b over the main dust plume). Since AE is inversely related to the mean particle size, the generally lower AE in ORG_NSPH implies the expanded presence of large dust particles in the air, demonstrating the effect of reduced particle sedimentation resulting from the non-spherical dust shape. We further perform statistical evaluation on model AE against VIIRS observations. Again, due to the absence of the marine aerosol effect in the WRF-Dust model, our statistical comparison focuses on the enclosed

region (i.e., dusty region) in Fig. 5b and c, where dust is dominantly present. In the bias evaluation (Fig. 6a and b), we compute the monthly mean AE bias of each simulation against the monthly mean observed AE. ORG_NSPH generates smaller biases than ORG_SPH in general. In the RMSE evaluation, we compute the RMSE of all the AE values at each grid point against the observed values at the same point over the simulation period; the results are shown in Fig. 6c and d. In general, ORG_NSPH has lower RMSEs over the dusty region than does ORG_SPH. The AE evaluation suggests the importance of dust shape in dust transport and particle size representation.

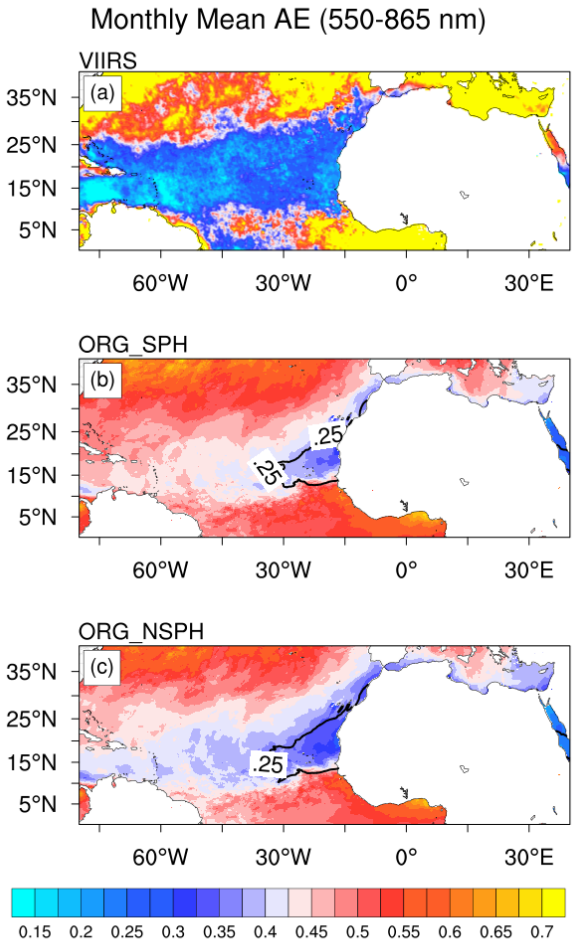

Fig. 5. *Monthly mean AE (550-865 nm) over ocean for July 2016. (a) VIIRS observed AE. (b-c) Modeled AE for the two dust shape numerical experiments: ORG_SPH and ORG_NSPH, respectively, superimposed by 0.25 modeled AOD contour lines, enclosing the region of high dust dominance.*

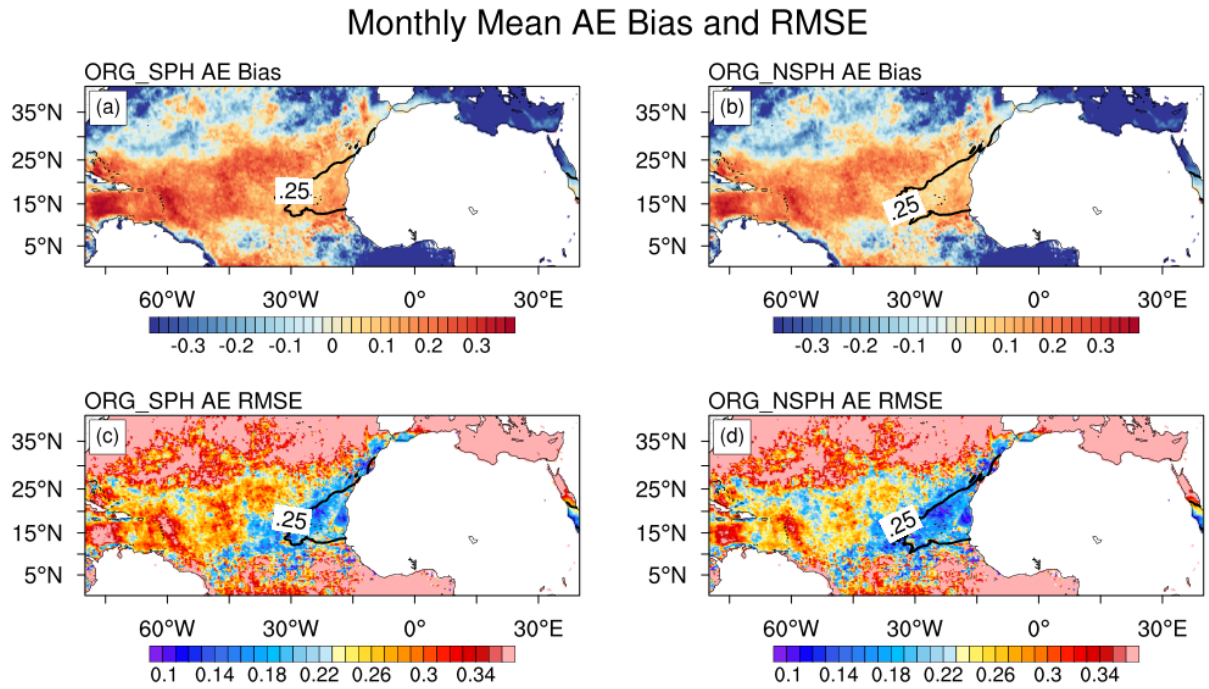

Fig. 6. *Statistical evaluation of experimental results against VIIRS AE observations. Panels (a) and (b) show monthly mean AE biases for the ORG_SPH and ORG_NSPH experiments. Panels (c) and (d) show the AE RMSEs. All the panels are superimposed by 0.25 modeled AOD contour lines.*

4.3. Emitted dust particle size distribution effect

4.3.1. Experimental design

The main focus of this set of experiments is the emitted dust particle size distribution, with the consideration of two different radiation schemes. We conduct four numerical experiments using different combinations of dust size distributions (ORG, GLO, and LOC) and radiation schemes (GSFC and FLG). The four experiments are ORG_GSFC, GLO_GSFC, LOC_GSFC, and LOC_FLG (Table 6). ORG_GSFC is our baseline case for comparison. The GLO_FLG experiment is excluded here, as this combination generated unreasonably low AE values (with occasional negative values) during model testing, which highly deviated from the observations and thus is excluded for comparison with other simulations. Further investigation and model adjustments will be conducted on the AE issue in the future.

Table 6. *The design of the four emitted dust particle size distribution numerical experiments.*

Size Distribution	Radiation Scheme	Experiment
ORG	GSFC	**ORG_GSFC**

GLO	GSFC	**GLO_GSFC**
LOC	GSFC	**LOC_GSFC**
LOC	FLG	**LOC_FLG**

As this set of experiments is built on the understanding of the impacts of dust shape in Section 4.2, the tri-axial dust shape assumption will be applied to all of the distribution experiments. Therefore, ORG_GSFC is, in fact, identical to ORG_NSPH in Section 4.2. The rest of the model setting follows the numerical configurations in Section 4.1, except that the LOC_FLG experiment utilizes 0.2 μg m^2 s^{-5} for the dimensional constant C, as opposed to 0.4 μg m^2 s^{-5} in the other experiments. The decision of halving the dimensional constant for LOC_FLG is necessary to account for the overshooting of optical depth values caused by the modified non-spherical optical properties for the FLG scheme (see Section 2.2.1). While a non-spherical area factor (γ) was used to account for the non-spherical effect on optical properties in the GSFC radiation scheme, the optical coefficients with the non-spherical effect in the FLG scheme were recalculated by Dr. Adebiyi's group using the OPAC software. With the modified optical coefficients, the AOD almost doubled in magnitude. Therefore, to adjust AOD close to observations, the emission was cut to half. Despite the modification in emissions, we found that AE and its errors remain largely unchanged (see Table 7 and Fig. 7). Thus, the LOC_FLG experiment may be fairly compared with the other experiments. Ultimately, we will verify the modified emissions against observations of dust mass or number concentration, as the model emissions are important in dust-cloud interaction.

Results from the numerical experiments will be compared with the observations to determine the model setting with the most accurate dust transport and size representation. This particular setting will be implemented in the Hurricane Earl's case study in Section 5. Since the modeled AOD can be modulated by adjusting the emissions via the dimensional constant C, it is more important that the model can accurately simulate AE, which is minimally affected by modeled emission fluxes. We will place greater emphasis on the AE evaluation of different emitted dust size distributions.

Table 7. *The same statistics as in Table 5, but for the LOC_FLG experiments with dimensional constants $C = 0.4$ μg m^2 s^{-5} and $C = 0.2$ μg m^2 s^{-5}. The comparison shows minimal differences in model AE errors.*

Experiment	AOD		AE	
	RMSE	MB	RMSE	MB
LOC_FLG, C = 0.4	0.501	0.098	0.161	0.007
LOC_FLG, C = 0.2	0.292	-0.175	0.160	0.008

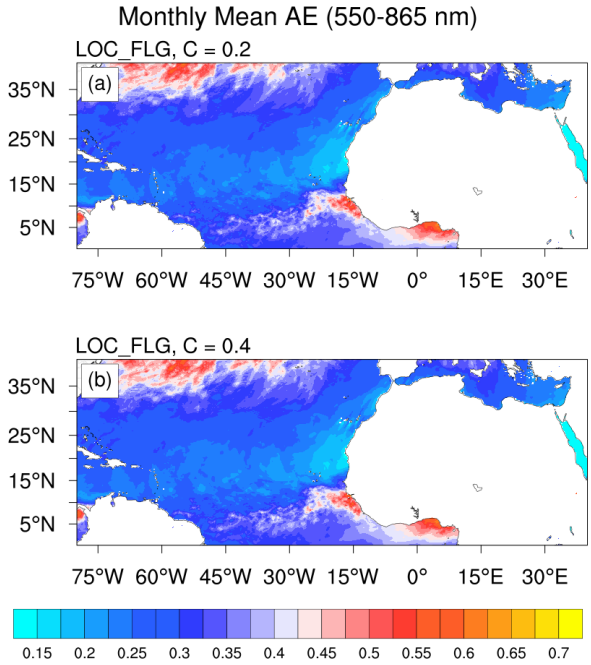

Fig. 7. *Monthly mean (July 2016) AE (550-865 nm) over ocean for (a) the LOC_FLG simulation with dimensional constant C = 0.2 μg m^2 s^{-5}, and (b) the same simulation setting but with C = 0.4 μg m^2 s^{-5}. The great similarity between the two settings shows the feasibility of modulating the modeled AOD by adjusting C, while maintaining nearly identical AE.*

4.3.2. Results and discussion

The model and AERONET AOD at 440 nm and AE at 440-870 nm for each AERONET site are examined in the form of time series (Fig. 8). The model data are presented at hourly intervals, whereas AERONET observations are reported at sporadic intervals during the daytime. Despite the differences in data frequency, the available observations and the general AOD and AE trends still provide a valid evaluation on model performance. Note again that since FDDA is used during these experiments, the meteorological features are optimized, and dust (i.e., AOD and AE) simulations among different experiments can be better evaluated with little influence from modeled meteorology.

The average particle size of a freshly emitted dust plume is generally greater than that of a plume that has travelled some distance because large particles settle faster and a higher fraction of coarse dust particles are still suspended in the air in a fresh dust plume. As a result, low AEs (~0.1-0.2) with high AODs are commonly recorded at near-source sites (ZA, BA, and DA). As dust plumes from Chad propagate downstream under the AEJ and AEWs, they may reach IC, DA, and CV. We can observe this phenomenon through the east-to-west propagation of local AOD maxima and AE minima over time in the time series—for example, AOD maxima and AE minima are recorded on 8 July at ZA, 9 July at BA, 11 July at IC, and 12 July at DA. In addition, the maximum AOD value decreases over time and distance from 1.2 at BA to 0.8 at DA; whereas the minimum AE value increases from nearly zero at ZA to 0.2 at DA. Contrary to the other sites, CV records relatively low AODs (~0.1-0.2) yet also low AEs throughout the month. The distinctive behavior of AOD and AE at CV can be ascribed to its oceanic location, being the only off-coast island site among our interested AERONET sites; as such, it is subject to marine aerosols from the surrounding ocean, which are large in particle size (low AE) but have a low average AOD of ~0.1 (Cuevas et al., 2015; Smirnov et al., 2009; Smirnov et al., 2011). Further experiments that account for soil erodibility and marine aerosols will be conducted to properly weight the contribution from both dust and marine aerosols.

As seen in the time series, our WRF-Dust model can generally reproduce the observed AOD and AE trends for all the experiments. For instance, for the previously discussed dust plume that propagates from its source in Chad to DA during 6-12 July, all the experiments can largely capture the trends as well as the timing of the maximum AOD and minimum AE. However, model performance in reproducing the observed AOD and AE features varies by experiment. Via integrating the LOC and GLO dust distributions, the model has shown considerable improvement in AOD and AE across all five AERONET sites. Specifically, the LOC and GLO experiments enhance the model AOD, which enables the model to more accurately capture high observed AOD values (e.g., 6-11 July at BA, ZA, and IC). Among the experiments, GLO_GSFC shows the greatest AOD enhancement. Yet, the augmentation of AOD may result in even more severe overestimation in the model. This is most pronounced at coastal sites (i.e., DA and CV).

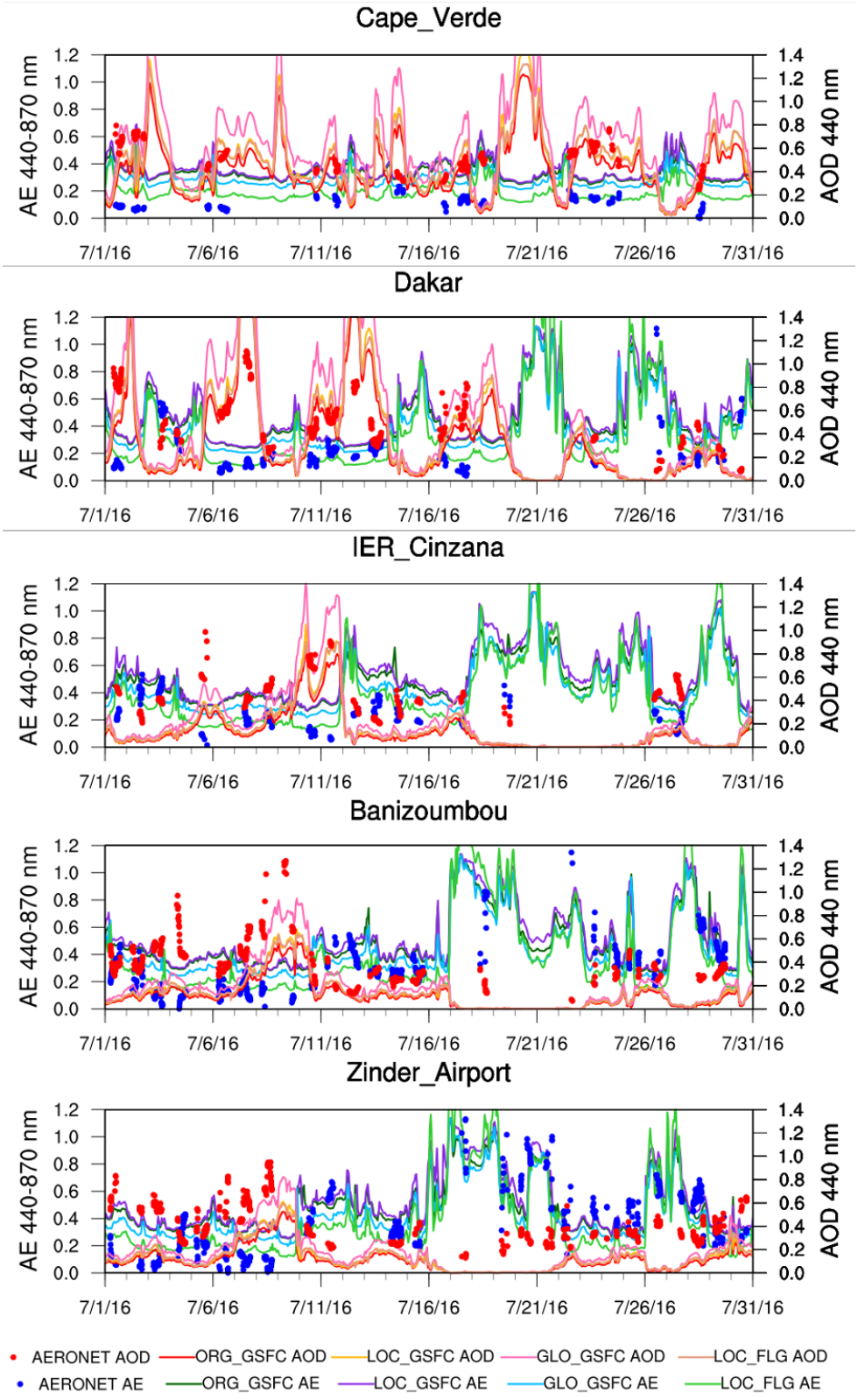

Fig. 8. *Time series of AERONET observed (dots) and modeled (lines) AE (440-870 nm) and AOD (440 nm) for July 2016 recorded at the following AERONET sites (from top to bottom): Cape Verde, Dakar, IER_Cinzana, Banizoumbou, and Zinder Airport.*

Additionally, the LOC_FLG and GLO_GSFC experiments display greater alignment in AE with the observations. The simulations largely reproduce low observed AEs compared to ORG_GSFC (e.g., 22-25 July at CV; 6-11 July at DA, IC, BA, and ZA), while still effectively capturing high observed AEs (e.g., 17-22 July at ZA). The alignment in AE is an indication of the model's improved ability to represent large dust particles. Based on our AE analysis, LOC_FLG best agrees with the AERONET measurements, followed by GLO_GSFC. LOC_GSFC, on the other hand, is comparable to ORG_GSFC in AE performance.

To quantitatively evaluate each experiment's results against all the valid AERONET data, we calculate the RMSE and bias. The statistical results are presented in Table 8. In the AOD RMSE evaluation, LOC_GSFC and LOC_FLG improve upon ORG_GSFC, while GLO_GSFC misses the observed AOD the most with the highest RMSE. The poor performance of GLO_GSFC is attributed to its severe overestimation of AOD, which will be further analyzed in the later evaluation against VIIRS observations. As mentioned earlier, the issue in AOD could be resolved by adjusting the dimensional constant in the model. In the AE evaluation, LOC_FLG generates the best model performance, with the smallest RMSE and MB among the experiments, followed by GLO_GSFC. This finding may be explained by the different optical properties in the radiation schemes (i.e., GSFC versus FLG). Also, LOC distribution accounts for dust emitted solely from our interested AERONET sites, while the GLO distribution could trivialize the contribution of Saharan dust in the process of global averaging. This is manifested in the weightings of model size bins—in the GLO distribution, less weighting in dust emissions is put on the largest size bin (see Table 2). LOC_GSFC, however, fails to improve AE simulation upon ORG_GSFC. Plausible reasons for the underperformance of AE in LOC_GSFC are that the contribution of the smallest bin is emphasized in the LOC emitted dust size distribution, but less so for the larger bins; and that our model size bins are capped at 10-μm diameter (see details in Section 2.2.2). These factors prevent the model from incorporating some of the most coarse dust particles (10-20 μm diameter) in LOC, leading to a higher emitted dust ratio for smaller particles than that if dust particles of 10-20 μm diameter were included. As a result, LOC_GSFC produces higher AE compared to other experiments. This finding also implies that the optical properties of

a radiation scheme can influence the modeled AE, since AE is an expression of the relation between AODs at two wavelengths. For instance, although sharing the same emitted dust size distribution as LOC_GSFC, LOC_FLG does not exhibit the overestimated AE issue. In fact, by implementing the FLG scheme, LOC_FLG simulates the lowest AE on average among the experiments. Thus, in addition to the emitted dust size distribution, the optical properties computed in a radiation scheme can be an important determinant of dust AE representation. Differences in optical properties may potentially arise from the following factors: 1) differences of spectral bands in the GSFC and FLG schemes, 2) the GSFC scheme's lumping of five bins into three modes in optical coefficient computation, and 3) different parameters used in the calculation of optical properties by the two radiation schemes.

Table 8. *The same statistics as in Table 5, but for the emitted dust particle size distribution experiments, including ORG_GSFC, GLO_GSFC, LOC_GSFC, and LOC_FLG. Note that ORG_GSFC is identical to ORG_NSPH.*

Experiment	**AOD**		**AE**	
	RMSE	MB	RMSE	MB
ORG_GSFC	0.305	-0.211	0.213	0.144
GLO_GSFC	0.351	-0.070	0.177	0.085
LOC_GSFC	0.304	-0.171	0.230	0.168
LOC_FLG	0.292	-0.175	0.160	0.008

Figure 9 depicts the monthly mean 550 nm AOD for the four emitted dust particle size distribution experiments. All the model simulations show an AOD pattern similar to the VIIRS observed pattern (see Fig. 4a). With the non-spherical dust particle effect considered, AOD with values of 0.2-0.3 in all the experiments extends to as far as 40°-50°W. In spite of the universal improvement in long-range dust transport and spatial dust distribution over the Atlantic, our WRF-Dust model consistently underestimates the AOD magnitude by 0.1-0.2 over ocean, which is close to the contribution by marine aerosols (inferred from the observed AOD outside the dust plume region). Nonetheless, the LOC and GLO experiments show varying degrees of improvement in AOD upon ORG_GSFC. On average, LOC_GSFC has a 24% increase in AOD over ocean compared to ORG_GSFC, LOC_FLG has a 24% increase, and GLO_GSFC has a 67% increase. Over land, our WRF-Dust model overestimates AOD in coastal dust hotspots near Mauritania at

15°W for all the experiments. With its drastic increase in overall AOD, GLO_GSFC exhibits the greatest overestimation across North Africa. The overestimation could be explained by the GLO distribution's high weighting on bins 2-4 compared to ORG and LOC. Dust particles in these bins have greater sustainability than those in the largest size bin, which settle faster; as such, the suspended dust particles can undergo dust-radiation interaction and enhance the modeled AOD. LOC_GSFC and LOC_FLG also show sizable overestimation at the African coast. Yet, the enhancement in modeled AOD allows LOC_GSFC and LOC_FLG to better reproduce the observed AOD over the Algeria region, which is underestimated in ORG_GSFC. For the Chad source region, our model is inadequate in reproducing the observed AOD, such that the modeled AOD is 0.2-0.35 lower than the observed. As discussed in Section 4.2.2, the dust source regions experience greater variability such that dust emissions are influenced by various meteorological factors, such as haboobs from local convective systems, which are not properly reproduced due to insufficient model resolution and model errors. The complexity poses a challenge in simulating AOD in those regions. Again, we may modulate the modeled AOD by properly adjusting the dimensional constant, model resolution, or incorporate soil erodibility to ameliorate coastal dust emissions.

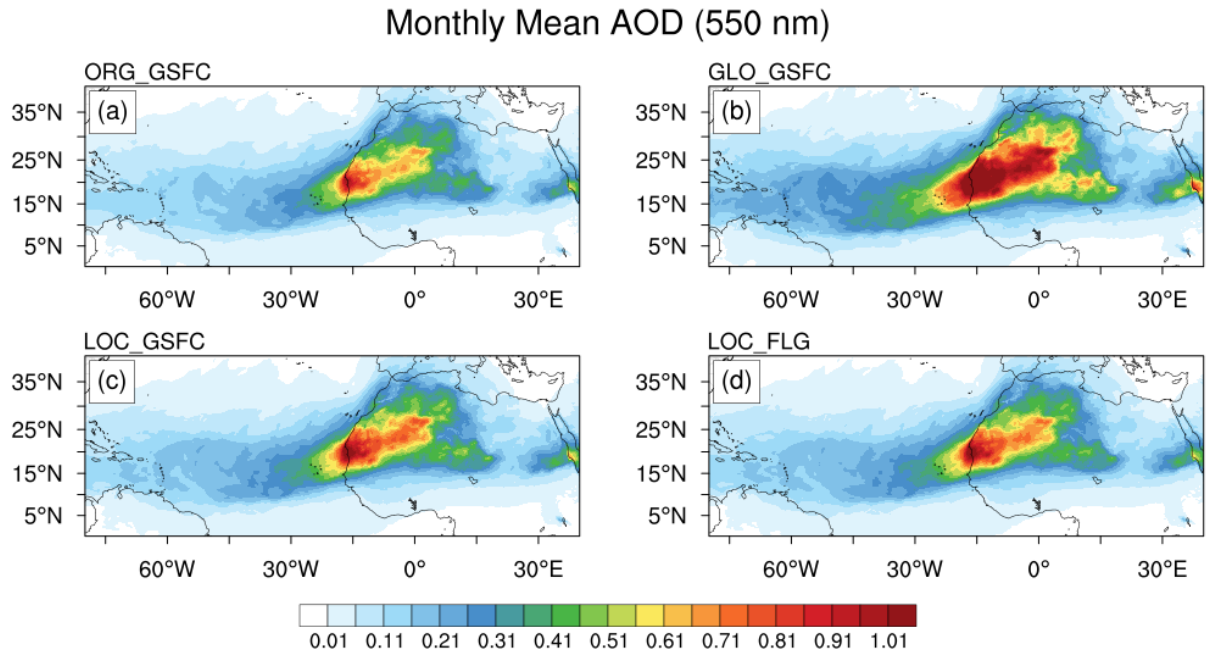

Fig. 9. *The same as Fig. 4, but for the emitted dust particle size distribution experiments, including (a) ORG_GSFC, (b) GLO_GSFC, (c) LOC_GSFC, (d) LOC_FLG. Note that ORG_GSFC is identical to ORG_NSPH.*

Figure 10 illustrates the monthly mean over-ocean 550-865 nm AE for the distribution experiments. A similar east-to-west monotonically increasing AE trend again appears in all the experiments. Compared to ORG_GSFC, GLO_GSFC and LOC_FLG show enhanced capabilities of transporting large particles from Saharan source regions out into the Atlantic. Particularly, in LOC_FLG, particles with AE of 0.1-0.2 can be seen near the West African coast, which is very similar to the VIIRS observed value of 0.1-0.25, implying that there is still a considerable fraction of large particles over this area. GLO_GSFC closely follows, with coastal AE of 0.25-0.3. On the other hand, ORG_GSFC and LOC_GSFC have the worst performance near the coast, with AE of 0.3-0.35. Further into the ocean up to the 0.25 AOD contour, LOC_FLG continues to transport and sustain particles with the lowest AEs (0.225-0.25) among the simulations. The VIIRS observed AEs (~0.1-0.25) remain very low throughout the dust-dominant region. Overall, LOC_FLG generates the best simulation performance in AE, with an average decrease of 46% in AE compared to ORG_GSFC.

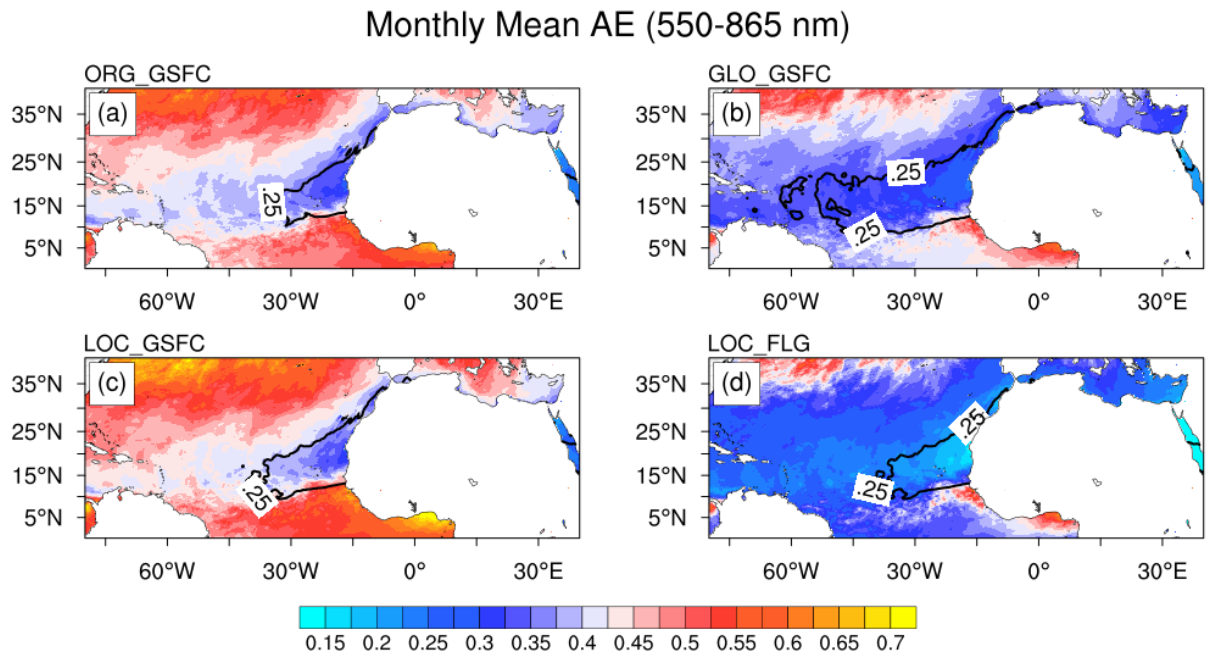

Fig. 10. *The same as Fig. 5, but for the emitted dust particle size distribution experiments. All the panels are superimposed by 0.25 modeled AOD contour lines.*

We apply the same statistics in Section 4.2.2 to evaluate modeled AE performance over ocean for all the distribution experiments. The statistical results are portrayed in monthly mean AE bias (Fig. 11a-d) and

monthly mean AE RMSE (Fig. 11e-h). The same conclusion as discussed earlier in the AERONET evaluation can be drawn using the statistics against the VIIRS observations—with the smallest RMSEs and MBs (close to 0), LOC_FLG is the best at reproducing the observed AE, whereas LOC_GSFC exhibits the least accurate AE simulation. Similar to the reason proposed for AE evaluation against AERONET observations over land, the overestimated AE in LOC_GSFC may be ascribed to the overemphasis of the smaller size bins in the LOC distribution, coupled with the optical properties in the GSFC scheme. Our AE analysis suggests that the combination of proper dust optical coefficients and accurate emission distribution is the key to keeping large dust particles aloft. Indeed, the non-spherical dust effect is equally important in slowing down the sedimentation of large particles and enhancing dust optical depth.

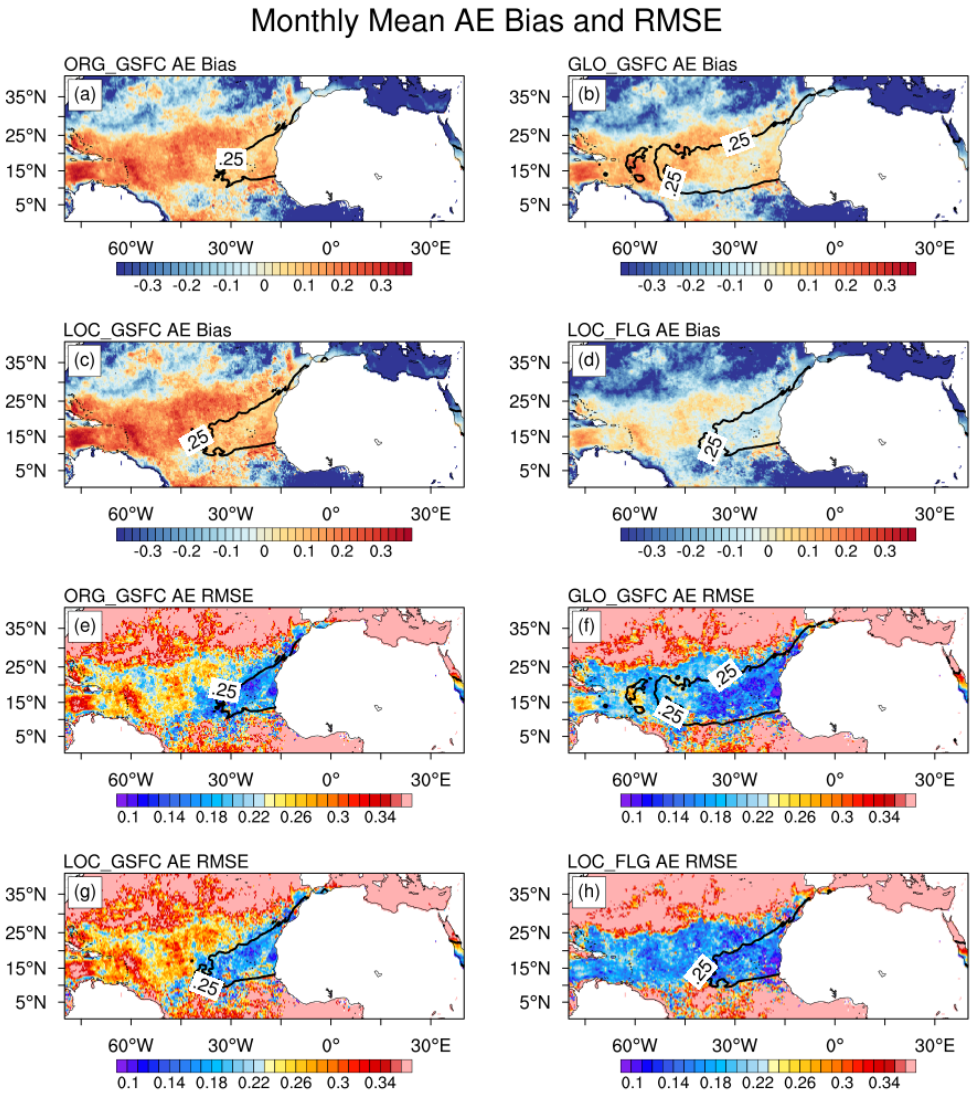

Fig. 11. *The same as Fig. 6, but for the emitted dust particle size distribution experiments. Panels (a-d): monthly mean AE bias. Panels (e-h): AE RMSE. All the panels are superimposed by 0.25 modeled AOD contour lines.*

The vertical distribution of dust is important to its interaction with both longwave and shortwave radiation, resulting in different static stability and horizontal temperature gradient (thus vertical shear). In addition, the dust-cloud interaction heavily relies on the height of a dust layer. Since AOD is a vertically integrated quantity, we will use vertical aerosol backscatter profiles from CALIOP to evaluate model vertical dust distribution. The details of the evaluation procedures are delineated in the following steps, similar to those in Choi et al. (2020):

1. Flag cloud-contaminated and unreliable CALIOP L2 total backscatter data by
   (a) selecting data points that are classified as "aerosol" or "clear air" by the CALIOP L2 vertical feature mask (VFM) product.
   (b) using only data points with extinction quality control (QC) flag values of 0, 1, 2, 16, 18, or 32,768 (Toth et al., 2018).

Note that the vertical resolution of both CALIOP L2 VFM and extinction QC data is finer (30 m) than that of CALIOP L2 total backscatter data (60 m), meaning that two VFM and extinction QC values exist for each backscatter value. Thus, a backscatter value is considered acceptable if both of its corresponding VFM values indicate "aerosol" or "clear air" and both of its associated extinction QC flag values are one or more of those listed in (b) above. Data that do not meet the criteria are flagged and assigned NaN values.

2. Compute model backscatter values for atmospheric gas molecules (derived from air pressure) and assign them to all valid CALIOP data points that are not flagged in the first step and do not have valid aerosol backscatter values. This step is different from that in Choi et al. (2020).
3. Average CALIOP backscatter data to model levels (i.e., superobs; Berger et al., 2004).

4. Interpolate modeled data to observational locations and utilize the forward operator of total backscatter from the Goddard Satellite Data Simulator (G-SDSU; Matsui et al., 2013; Matsui et al., 2014) to transform modeled dust and gases into backscatter data.
5. Interpolate backscatter data to the same heights for all columns and perform statistical comparison between CALIOP and modeled vertical profiles.

Figures 12b and c portray an example of CALIOP-observed and modeled vertical backscatter profiles (from the LOC_FLG simulation) along two specific CALIOP tracks indicated in Fig. 12a. In this example, we select CALIOP swaths at 0300 UTC 17 July within a 3-hour time window (±1.5 hours). We follow the procedures above to obtain the observed vertical cross sections of aerosol backscatter as well as the modeled cross sections along the same tracks via the G-SDSU. Note that the selected case is one of the best cases that exhibits great similarity between the modeled and observed backscatter cross sections. The procedures are repeated for the entire simulation period and applied to all numerical experiments. We compute the RMSE and model bias of the monthly averaged simulated backscatter profiles against the CALIOP backscatter profiles.

The statistical analysis results are displayed in Fig. 13. The model shows the greatest deviation at 0-1 km for all the experiments, reflected by the large RMSE and negative bias values over the same altitudes. From 1-6 km, different simulations reproduce the observed backscatter with various degrees of accuracy. LOC_FLG consistently underestimates the observation up to 6 km in part due to the reduction of the dimensional constant C, while the other simulations mostly overestimate the observed backscatter. LOC_FLG shows the greatest resemblance to the observation at 2-4 km, followed by ORG_GSFC and LOC_GSFC. GLO_GSFC, on the other hand, has the largest absolute bias due to its overestimation. In contrast to the varying biases, the RMSEs are nearly identical across all the simulations, except that GLO_GSFC has slightly larger RMSE at 1.5-5 km, since it has more errors in larger magnitudes. The error can be potentially reduced by assimilating AOD and backscatter data. In the mean absolute error (MAE) profiles, LOC_FLG generally generates the least error among all the experiments, followed by ORG_GSFC,

LOC_GSFC, and GLO_GSFC. Overall, the model simulations possess the greater RMSEs and biases near the surface, dwindling with increasing height.

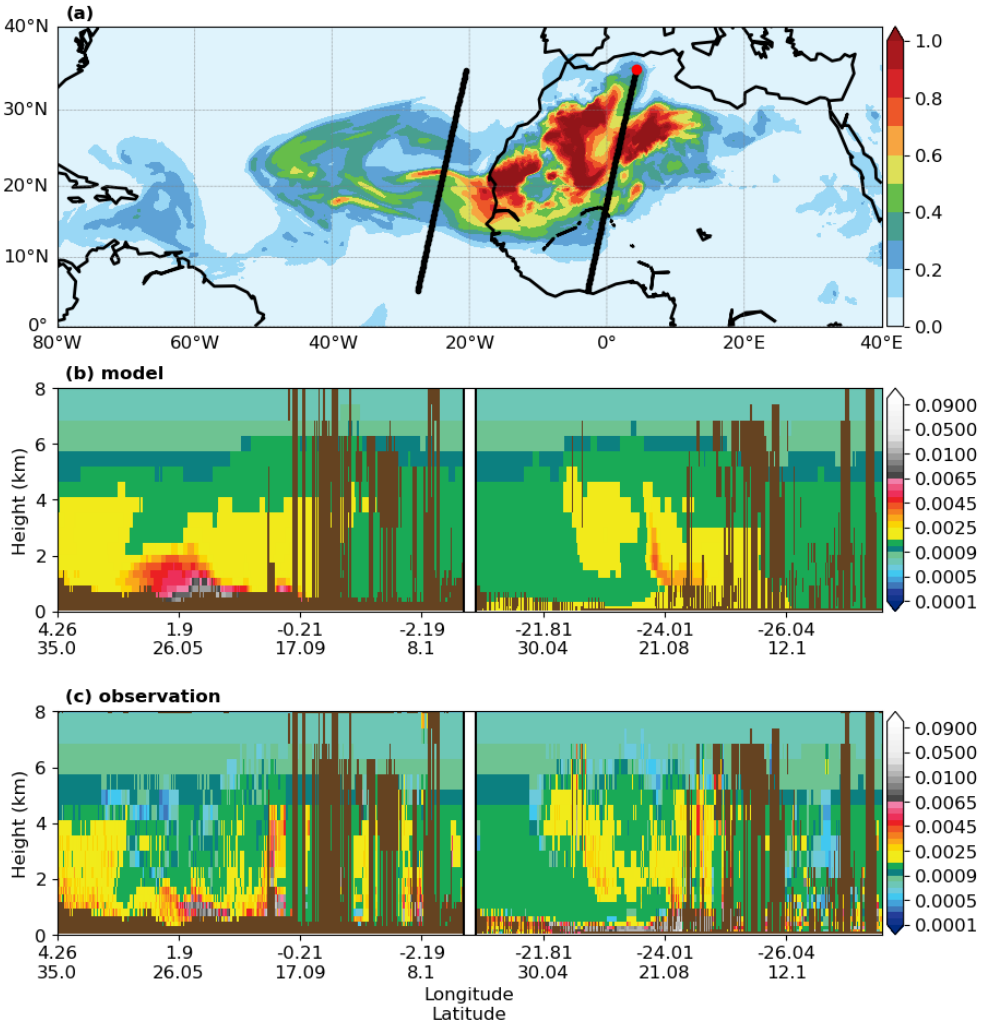

Fig. 12. *(a) The CALIOP satellite tracks at 0300 UTC 17 July (±1.5 hours), overlaid with the modeled (LOC_FLG) AOD at the same time. Note that the red dot denotes the starting point of the track. (b) The modeled vertical cross sections of aerosol backscatter (km^{-1} sr^{-1}) along the satellite tracks in (a). (c) The same as (b), but for the CALIOP observation.*

In conclusion, LOC_FLG can best replicate AERONET observations over land, generating the smallest RMSE and MB in AE and the smallest RMSE in AOD. The same conclusion applies in the evaluation over ocean, where LOC_FLG is able to reproduce low coastal AE values (0.1-0.2) and the westward extension of low AEs into the Atlantic Ocean, which best agrees with the VIIRS observations among all the simulations. GLO_GSFC follows LOC_FLG in AE performance, yet it strongly overestimates AOD. In the

backscatter evaluation against CALIOP observations, LOC_FLG generates the smallest MAE and highly resembles the observed profile over 2-4 km. However, it also has the greatest errors (e.g., RMSE) from the observations near the surface (0-1.5 km), which necessitates further analysis. Based on the findings above, we conclude that LOC_FLG produces the best model performance in dust representation.

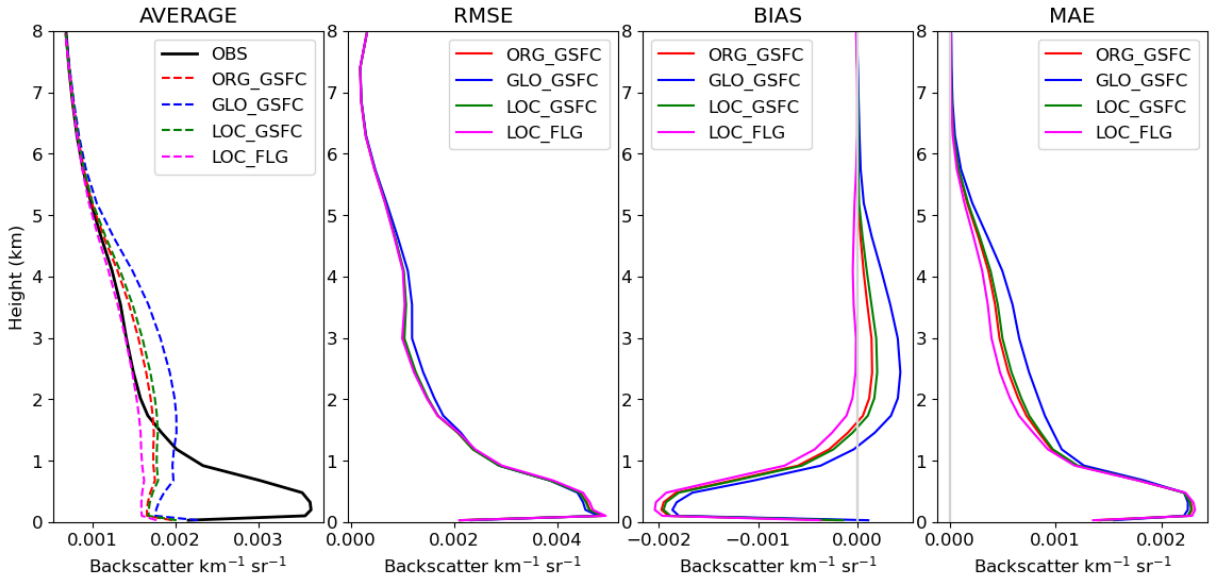

Fig. 13. *Monthly mean (July 2016) vertical profiles of, from left to right, average, RMSE, bias, and MAE of backscatter (km^{-1} sr^{-1}) for the CALIOP observations and the dust distribution experiments. Statistics are calculated against CALIOP backscatter observations passing over the same locations as in the model.*

5. Effect of improved dust simulation on model meteorology

5.1. Case study of Hurricane Earl (2010)

Dust has an important impact on weather systems through dust-radiation and dust-cloud interactions as discussed in the introduction. With our modifications of the dust particle shape and emitted dust particle size distribution, we have improved dust simulation in the aspects of optical properties and particle size representation. In order to investigate whether the improved dust simulation would lead to improvement of model meteorology, we conduct a case study on Hurricane Earl (2010). Hurricane Earl was a major hurricane that originated from a strong tropical wave near Cape Verde on 23 August, underwent rapid intensification on 29 August, reached its peak intensity as a Category 4 hurricane on 2 September, and eventually dissipated and became extratropical on 4 September. Due to the hurricane's origin in Africa,

dust can play a key role in the hurricane's development. The ability of the WRF-Dust model to reproduce the hurricane's environment, track, and intensity is one of the main criteria to evaluate model improvement with the modifications.

5.1.1. Experimental design

We apply the best configuration from Section 4 (i.e., LOC_FLG) to conduct the study on Hurricane Earl. The best configuration is, again, compared to the baseline experiment (i.e., ORG_GSFC). Thus, we conduct two numerical experiments for this case study. The Hurricane Earl case study consists of an 11-day simulation period (20-31 August 2010), encompassing the hurricane's genesis and development into a major hurricane. The domain configuration consists of three domains, with horizontal resolutions of 12 (d01), 4 (d02), and 4 (d03) km, respectively (see Fig. 14). Domain 1 (d01; 105°W-40°E, 10°S-55°N) is the parent domain covering the general area of interest (Africa and the Atlantic Ocean). Domain 2 (d02; 40°W-0°, 5°N-27°N) and domain 3 (d03; 75°W-37.5W°, 5°N-27°N) are two child domains placed on the hurricane track to simulate the development and intensification of Earl with their high resolution. The simulation time and nudging strategy differ for different domains depending on their respective purposes. The model runs on d01 for the entire simulation. Since an 11-day forecast is considered too long for a free regional model run, FDDA is applied to d01 for the initial four days to ensure that dust propagates to the eastern Atlantic Ocean along with the storm under reasonable meteorological conditions (e.g., AEJ and AEWs). The remaining seven days are simulated under free run (i.e., no nudging applied), so that the model may simulate the intensification of Earl and the differences between the two experiments can appear if they exist. Domain 2 spans over 20-28 August to cover the beginning portion of Earl's track. As d02 starts at the same initial time as d01, the four-day spectral nudging is required for d02. Wavelengths longer than 500 km are nudged to the reanalysis data. Domain 3 is not activated until Earl enters d02's eastern boundary. Thus, d03 runs during 27-31 August, and no nudging is implemented. The resulting simulated hurricane and related meteorological fields of the two experiments will be analyzed and compared to quantify any improvement due to the improved dust model configuration.

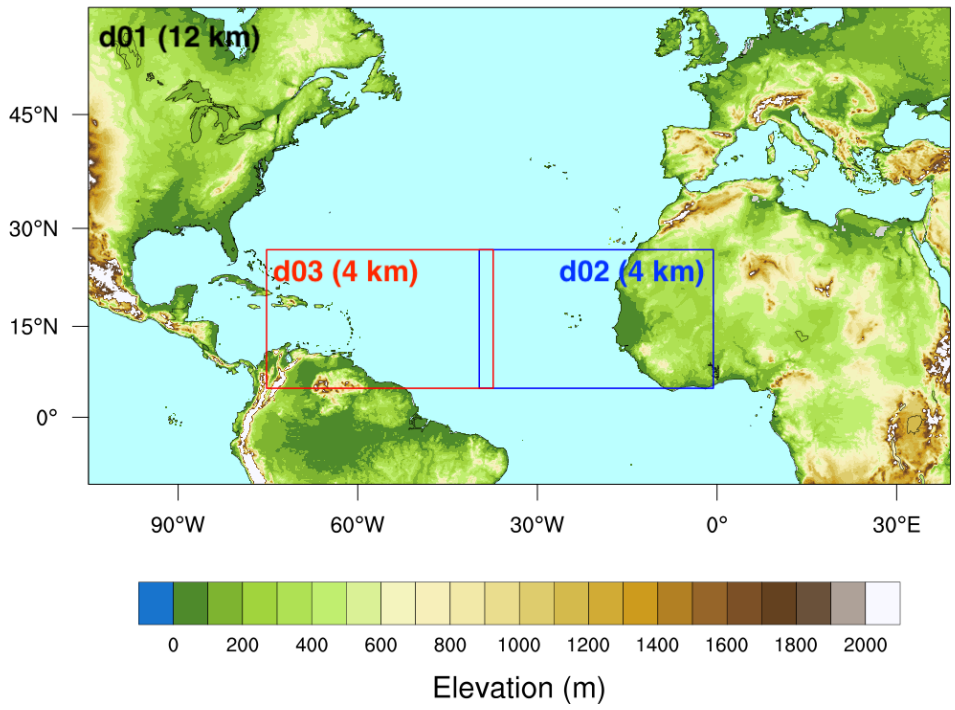

Fig. 14. *Domain configuration for the study of Hurricane Earl (2010). Domain 1 (d01) is the parent domain, with horizontal resolution of 12 km. Domains 2 and 3 (d02 and d03) are the two child domains, with resolution of 4 km, placed over the cyclone's track.*

5.1.2. Results and discussion

Before analyzing the simulated meteorological fields and hurricane tracks, it is important to first examine the modeled AOD to see if there is improvement in dust associated with the LOC_FLG configuration. Figure 15 shows the MODIS observed AOD and the modeled AOD for both ORG_GSFC and LOC_FLG experiments at 1500 UTC 28 August 2010 (after 207-h simulation, including 4-day nudging) as an example. In comparison to ORG_GSFC (Fig. 15d), higher AOD values are seen off the African coast (20°N, 15°W), over the source region of Chad (10-30°N, 0-25°E), and around the cyclone (20-25°N, 40-50°W). The slightly enhanced AOD at the western coast (15-20°N) and around the storm in LOC_FLG is better aligned with the observed AOD, indicating the simulation's improved ability to transport dust into the Atlantic Ocean. At the northwestern African coast (30°N, 10°W), ORG_GSFC simulates higher AOD than LOC_FLG. Yet, the observed AOD is low at this location, indicating that ORG_GSFC has stronger overestimation there compared to LOC_FLG. Outside the northwestern coast (20-30°N, 20°W),

ORG_GSFC also simulates higher AOD, which is closer to the observed values. Overall, LOC_FLG slightly better agrees with the MODIS observations, in particular at the western coast and north of the storm where the major dust plume extends farther west (Fig. 15d), although neither simulation reproduces adequate AOD off the coast and around the hurricane.

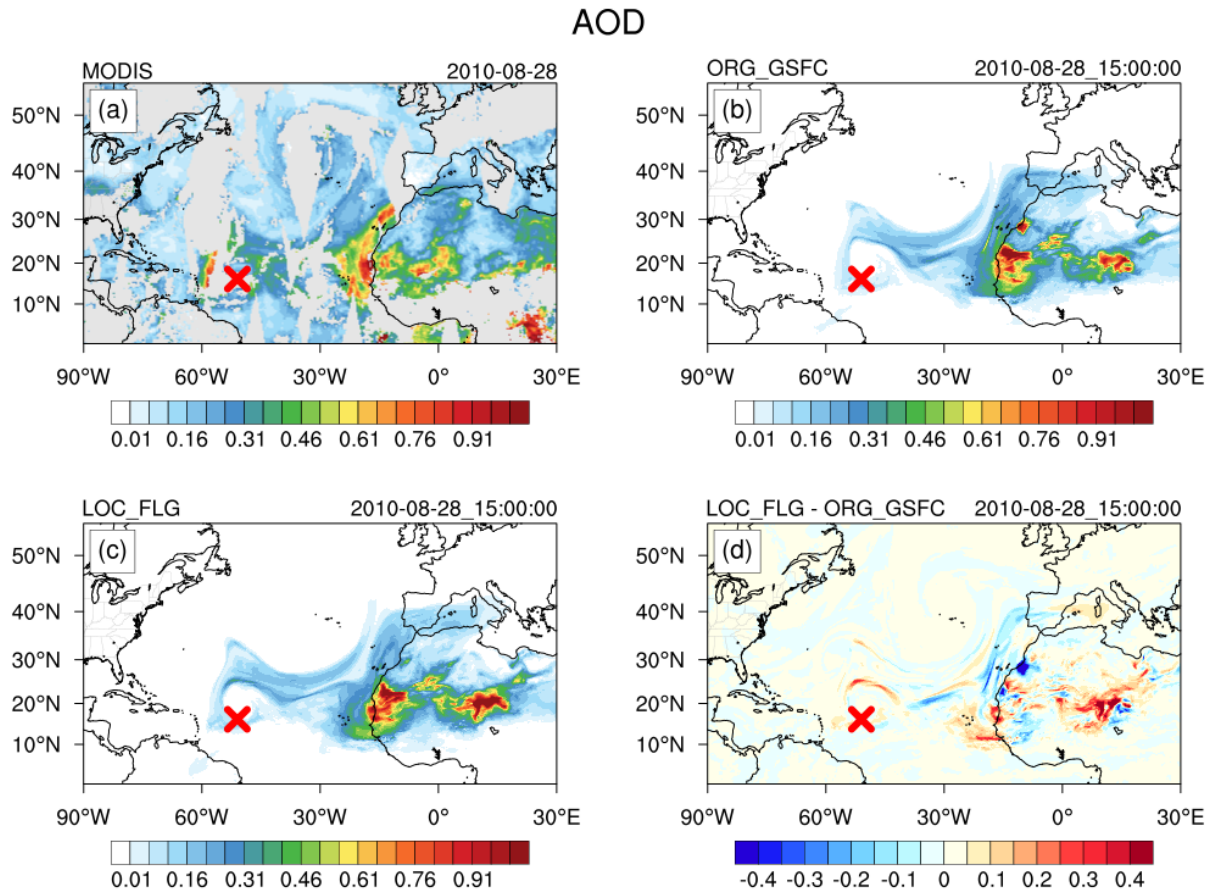

Fig. 15. *AOD (550 nm) over the region of interest from (a) MODIS observation on 28 August 2010, (b) ORG_GSFC simulation, and (c) LOC_FLG simulation at 1500 UTC 28 August 2010 (204-h simulation, 4-day nudging included). The model time chosen is close to the time at which the MODIS satellite swath passes over Hurricane Earl. Panel (d) depicts the AOD differences of LOC_FLG – ORG_GSFC. The cross on each panel denotes the observed location of Hurricane Earl.*

The impacts of the improved AOD field on temperature and wind profiles are analyzed. Figure 16 depicts the 750-, 850-, and 950-hPa temperature fields for the ERA5 reanalysis and model biases at 1200 UTC 28 August 2010 (108-h simulation into the free run). In general, compared to LOC_FLG, ORG_GSFC shows colder biases against ERA5 reanalysis over North Africa throughout all three pressure levels as well

as slightly colder biases near Hurricane Earl at 750 and 850 hPa. One of the reasons for the model cold biases is insufficient heating by dust. Over land, the severe cold bias in ORG_GSFC is further complicated by the GSFC scheme's optical properties leading to model cold bias. In the LOC_FLG simulation, on the other hand, somewhat warmer biases can be seen at 15°N over land and near the coast across the three levels. Moreover, both experiments present warm biases at 950 hPa over the central to western Atlantic, which implies that the vertical distribution of dust could be problematic after long-range transport.

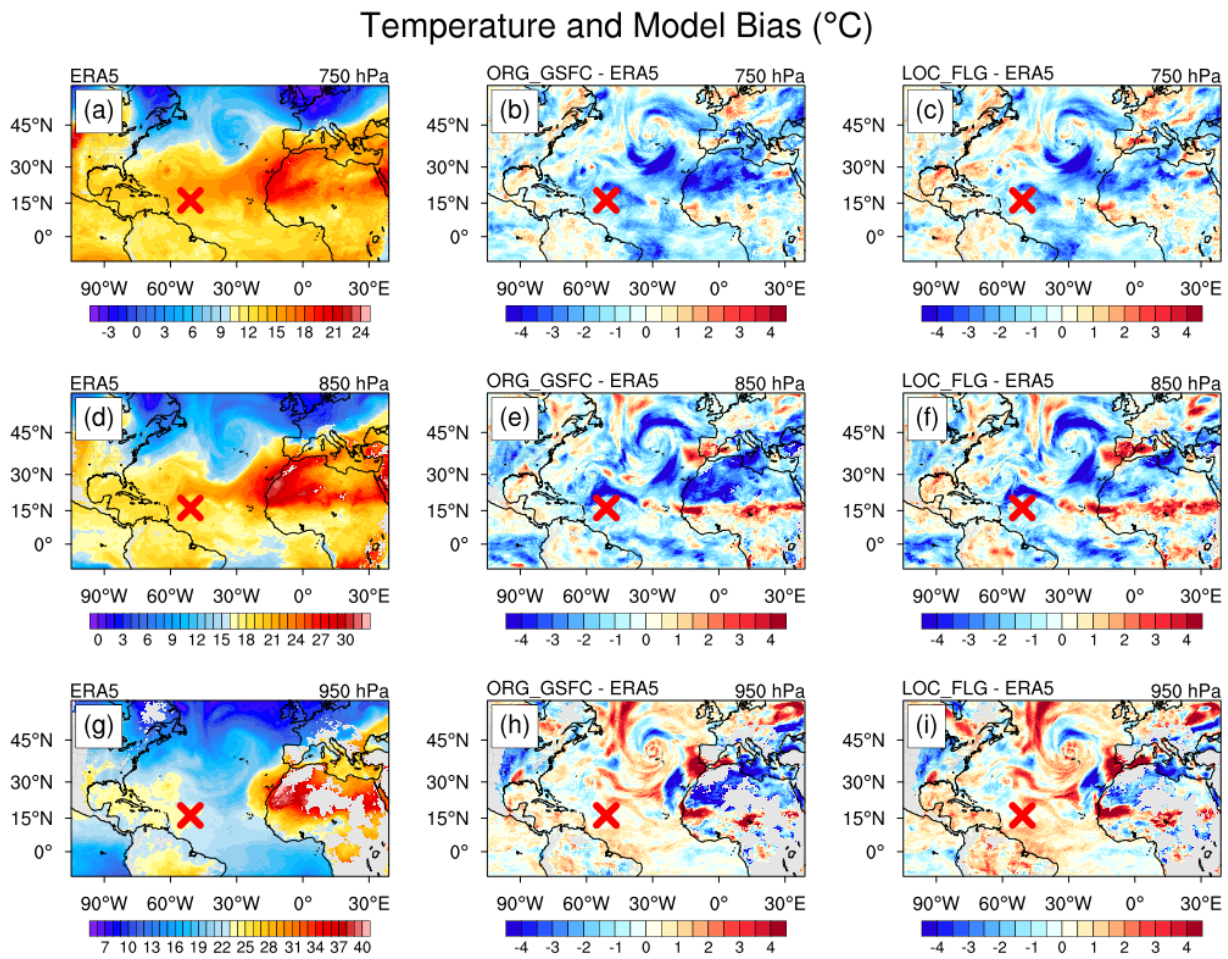

Fig. 16. *(a) Temperature at the 750-hPa pressure level at 1200 UTC 28 August 2010 for the ERA5 reanalysis data. (b-c) Model temperature bias from the ERA5 reanalysis 750-hPa temperature for the ORG_GSFC and LOC_FLG simulations, respectively. (d-f) The same as (a-c), but at 850 hPa. (g-i) The same as (a-c), but at 950 hPa. The cross on each panel denotes the observed location of Hurricane Earl.*

To investigate whether the GSFC radiation scheme's optical properties contribute to the cold bias over North Africa, we conducted a quick test which used the FLG radiation scheme while maintaining the ORG

size distribution (i.e., ORG_FLG) and compared the simulated AOD, temperature, and wind shear with those of LOC_FLG. Figure 17a shows that LOC_FLG simulates higher AOD than ORG_FLG in Chad, coastal Africa, and the northern band of Earl, similar to the comparison between LOC_FLG and ORG_GSFC, suggesting that the LOC distribution helps transport more dust into the storm region, regardless of the radiation scheme chosen. Figure 17b shows minimal positive temperature differences (LOC_FLG – ORG_FLG) over land at 850 hPa, which are consistent with the small positive AOD differences, in contrast to the much colder bias over land in ORG_GSFC. This finding suggests that in addition to the dust amount, the radiation scheme chosen, in particular its associated optical properties (e.g., the dust absorption-to-scattering ratio), could have an impact on modeled temperature, especially over land where dust concentration is high. The difference of the heating effect associated with dust is examined in an east-west vertical cross section over the maximum AOD difference region (19°N, 15°W – 19°N, 10°E; see Fig. 17c). There is clear dust-induced heating below 600 hPa, as evidenced by the general alignment between positive total dust differences and positive temperature differences. The total dust differences at 19°N are again examined together with the wind shear differences at 17°N (Fig. 17d), since the maximum AOD difference at 19°N induces the greatest difference in heating there by dust, creating the maximum temperature difference gradient slightly south of the main dust plume at ~17°N. Over 500-700 hPa, the positive total dust differences are somewhat correlated to the negative wind shear differences, indicating that dust-induced heating indeed influences the winds to a certain degree via thermal wind relation. Nonetheless, this alignment between dust and wind shear differences is relatively weak and not as evident as the relation between dust and temperature differences because winds are simultaneously controlled by different mechanisms, such as momentum advection, in addition to the dust-radiative effect.

Figure 18 illustrates wind speeds at 650- and 950-hPa levels as well as their resulting wind shear for the ERA5 reanalysis and model simulations at 204 h. Vertical wind shear is one of the key components that influences hurricane development, as it directly affects the core and structure of a hurricane. Both the ORG_GSFC and LOC_FLG simulations largely capture the ERA5 reanalysis wind patterns at both levels. However, at 650 hPa, the level at which the maximum magnitude of the AEJ is typically observed, our

model underestimates winds at the storm region and off the African coast at 15°N and overestimates in the south near the equator. The wind underestimation might be again related to the underestimated AOD, which results in less dust heating and reduced horizontal temperature gradient. Also, the southward shift of the AEJ has long been a problem in numerical modeling. The higher AOD off the African coast has a positive impact on winds in LOC_FLG, augmenting the wind speed slightly closer to the ERA5 wind speed near 5-20°N, 15°W at 650 hPa and near 15-22°N, 15°W at 950 hPa. Similarly, in the wind shear analysis, LOC_FLG exhibits stronger wind shear than does ORG_GSFC at 0-30°N. Unlike temperature, there is little to no wind or wind shear improvement associated with the improved AOD over the hurricane region. The impact of AOD improvement on wind is nearly nonexistent since dust does not directly alter atmospheric winds but through the thermal wind relation, as discussed earlier in the wind shear difference cross section. Thus, the model uncertainty might dominate the difference of dust-radiative contribution to the wind improvement.

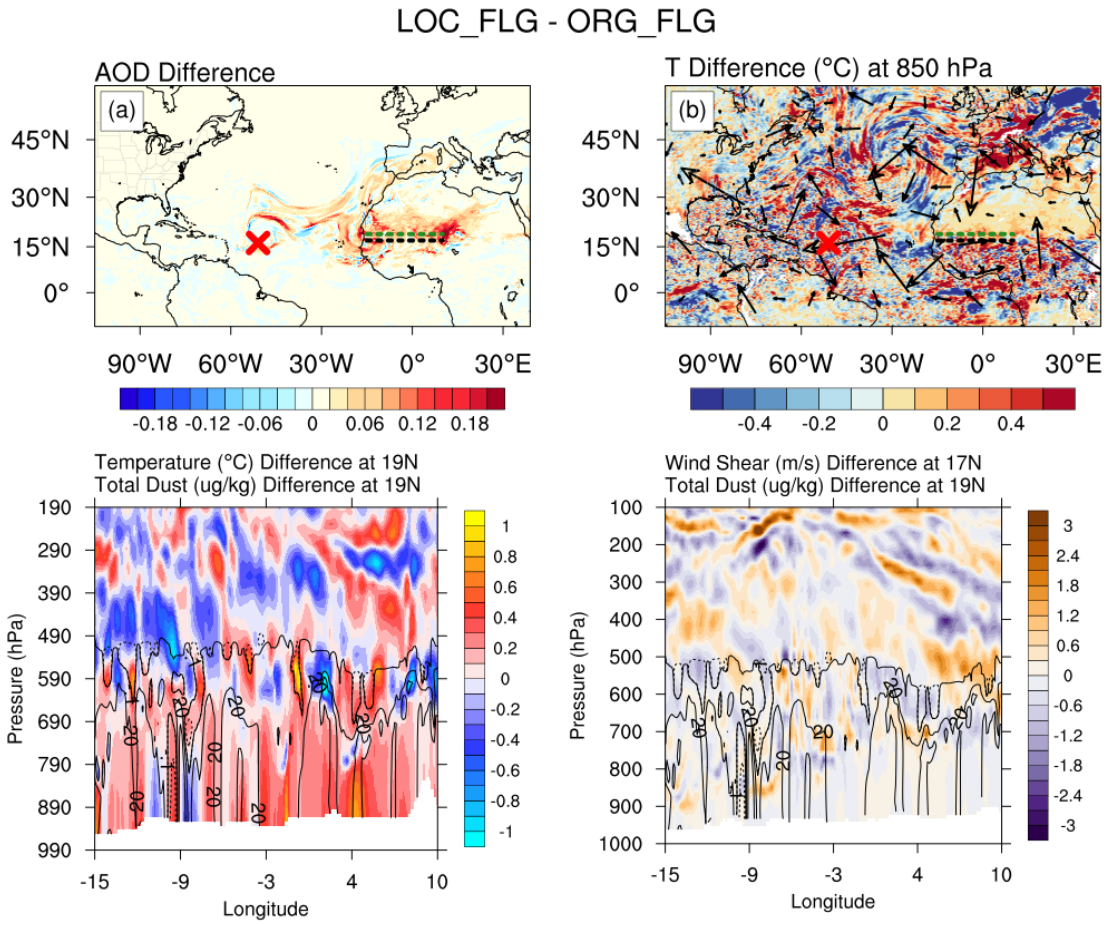

Fig. 17. *Various differences (LOC_FLG – ORG_FLG) at 1200 UTC 28 August 2010 (204-h simulation). (a) AOD differences. (b) Temperature differences (°C) at 850-hPa pressure level, superimposed by the wind vector differences. The cross denotes the observed location of Hurricane Earl. (c) Cross section of temperature (°C; shading) and total dust (μg/kg; solid contour lines denote positive differences and dotted contour lines denote negative differences) differences over the green dotted segments in (a) and (b) (19°N, 15°W – 19°N, 10°E). (d) Cross section of wind shear differences (m/s; shading) over the black dotted segments in (a) and (b) (17°N, 15°W – 17°N, 10°E) and, again, total dust differences over the green dotted segments.*

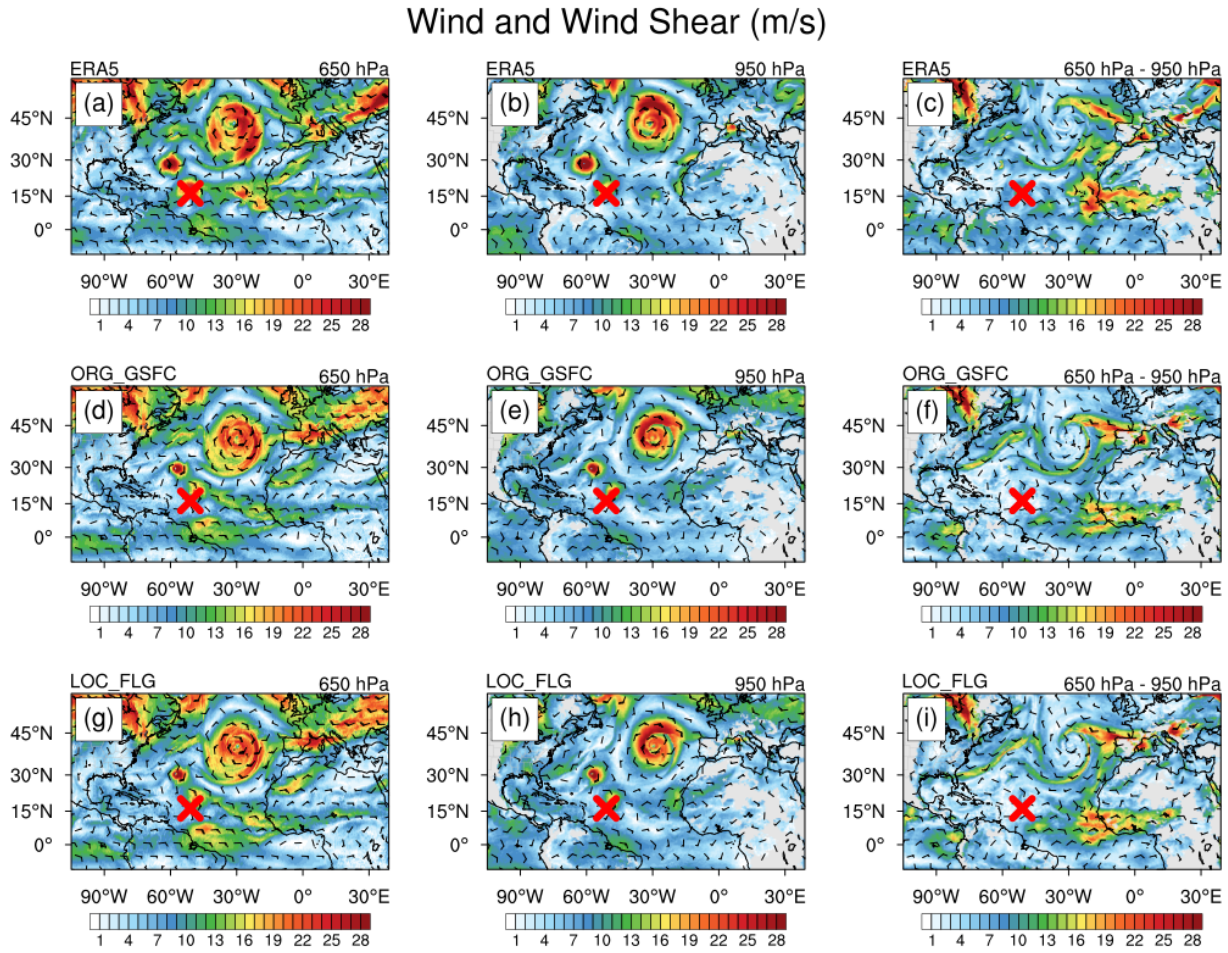

Fig. 18. *(a-b) Wind speed at 1200 UTC 28 August 2010 for the ERA5 reanalysis data at the 650-hPa and 950-hPa pressure levels, respectively. (c) The corresponding wind shear (i.e., the difference of 650-hPa and 950-hPa winds). (d-f) The same as (a-c), but for the ORG_GSFC simulation. (g-i) The same as (a-c), but for the LOC_FLG simulation. The cross on each panel denotes the observed location of Hurricane Earl.*

Figure 19a portrays the observed [best track data from the National Hurricane Center (Cangialosi 2011)] and model simulated storm tracks of Hurricane Earl. The tracks are represented by the locations of the

storm's minimum sea level pressure (MSLP) at six-hourly intervals from 1200 UTC 24 August to 0000 UTC 31 August. The two model simulated tracks share great similarity in position. Both tracks start deviating from the observed track from 1200 UTC 27 August (60 hours after the end of reanalysis nudging), after which the simulated tracks propagate northwestward, while the observed track continues to the west. Based on the sea level pressure analysis (not shown here), there is a stronger subtropical high in our model simulations, about 4 mb higher than the ERA5 reanalysis, despite the location being roughly the same. The stronger subtropical high can more effectively steer the hurricane northward along its edge. In addition, the mid-level winds (e.g., 500-hPa winds) can steer the hurricane's movement and thus modulate its track. Our model simulated mid-level winds having a greater south-north component than the ERA5 reanalysis, in part because of insufficient long-range dust transport at middle levels, can also contribute to track error. These factors together cause our simulated tracks to take a northward turn.

Figures 19b and c show the MSLP and maximum 10-m wind speed of the hurricane, respectively. The ORG_GSFC and LOC_FLG simulations overall show similar MSLP and wind speed. Starting from 0000 UTC 27 August, LOC_FLG consistently simulates greater intensity in MSLP (~4 hPa lower on average) and wind speed (~3 m/s higher on average) compared to ORG_GSFC. The model simulated storm's MSLP and wind speed magnitude are comparable with the best track observations until 1200 UTC 29 August. Starting from this time, Hurricane Earl underwent rapid intensification; the observed MSLP dropped sharply from 985 mb at 1200 UTC 29 August to 938 mb at 0000 UTC 31 August and the maximum 10-m wind speed increased drastically from 33 m/s to 59 m/s over the same period. Our model fails to reproduce this rapid intensification. The simulated tracks deviating into the colder water in the north further dampens the modeled storm intensity. In addition, the model cannot well simulate convective cloud processes with 4-km resolution. Higher resolution (e.g., 1 km) might be required. On the other hand, the problems in the storm track may partially stem from the inaccurate representation of the subtropical high and insufficient dust over the storm region in the model, suggesting that the modified configuration is still inadequate in enhancing the dust-radiation interaction and transporting dust sufficiently far into the ocean. Adjusting the dimensional constant and incorporating larger size bins (i.e., accounting for 10-20 μm dust particles) are

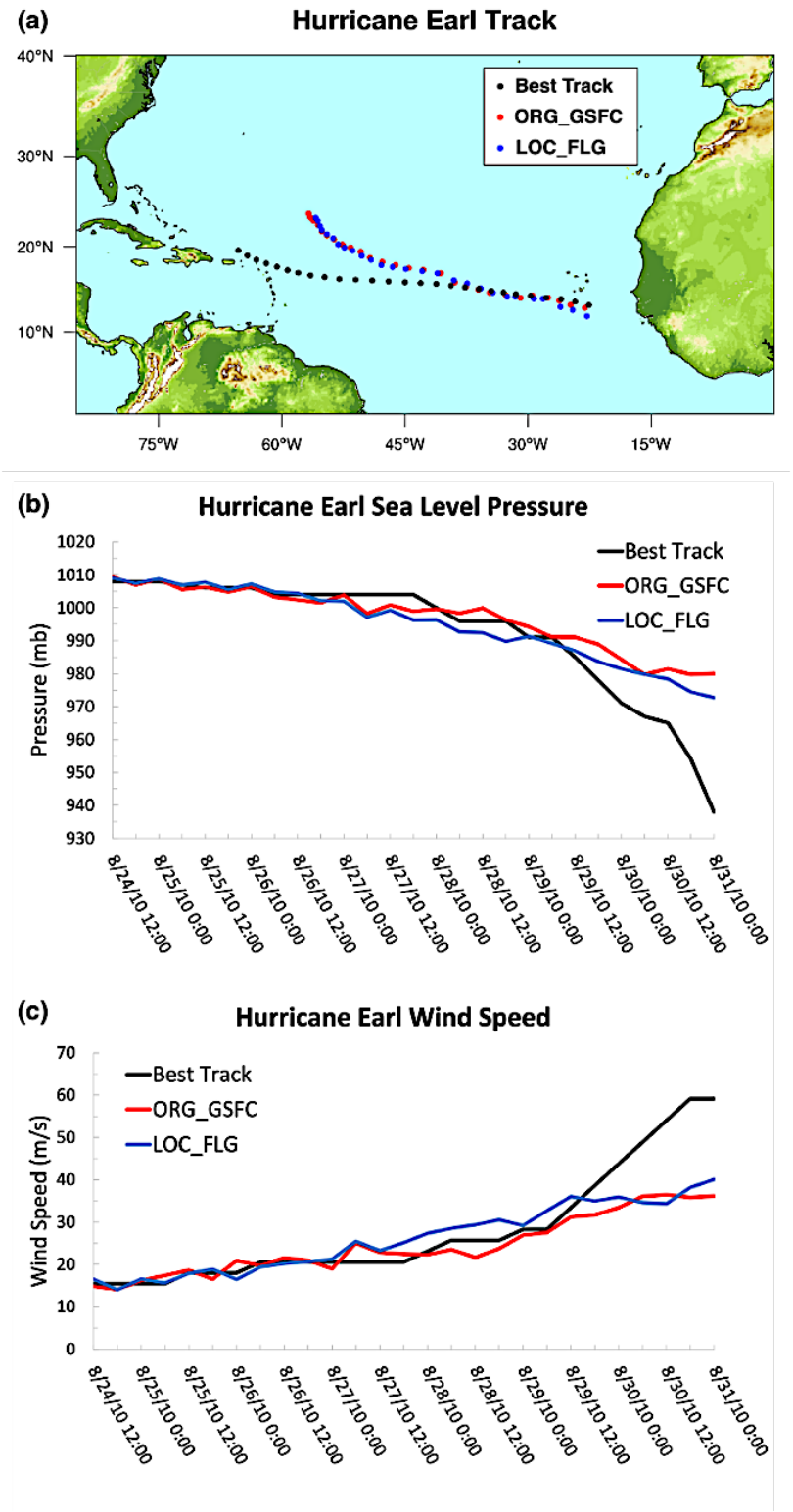

Fig. 19. *(a) Hurricane Earl's storm tracks from the National Hurricane Center best track data, ORG_GSFC, and LOC_FLG model simulations. The tracks cover the period of 1200 UTC 24 August – 0000 UTC 31 August 2010. Note that the dots represent the hurricane's locations at six-hourly intervals. (b) Minimum sea level pressure of Hurricane Earl from the best track data, ORG_GSFC, and LOC_FLG over the same period as the storm tracks. (c) The same as (b), but for the maximum 10-m wind speed.*

some potential approaches to ameliorate dust simulation. Yet, dust is not the sole determinant in the hurricane's development and its surrounding environment. The closely preceding Hurricane Danielle (2010) has a substantial influence on Hurricane Earl's environment, which adds further complication to our model simulations. Eventually, we may need to implement data assimilation to improve the storm representation. Overall, the LOC_FLG simulation shows slight improvement in AOD, leading to mildly improved temperature off the African coast and over the storm region. Although the LOC_FLG simulation slightly increases the storm intensity in terms of MSLP and 10-m wind speed, their differences might not be meaningful. Further investigation on the storm track and rapid intensification is required to draw a sound conclusion.

6. Summary

In this study, the overarching objective is to improve dust modeling through integrating non-spherical (tri-axial ellipsoidal) dust particle shape and observationally-constrained dust emitted size distributions, in an effort to tackle common dust modeling issues including early dust sedimentation, underestimated dust-radiative effect, and insufficient dust long-range transport. Modeled dust non-sphericity is characterized by shape factors averaged from field campaign data. Incorporating the non-spherical shape factors helped to effectively reduce dust particles' settling velocity and enhance dust optical properties. Regarding the emitted dust size distribution, we constrained the model distribution with global (GLO) and local (LOC; specific to our study region) in situ measurements and ensemble model simulations. We conducted two sets of sensitivity numerical experiments over North Africa in July 2016 to assess the impacts of non-spherical dust shape and constrained dust size distributions on dust simulation. Since dust has an important influence on weather and climate through dust-cloud and dust-radiation interactions, we applied the best numerical setting to conduct a study on Hurricane Earl (2010) to evaluate the improvement of modeled meteorological fields as a result of improved dust simulation.

In the dust particle shape experiments, the ORG_NSPH simulation (i.e., the original distribution with non-spherical dust shape considered) shows better performance than ORG_SPH, its spherical shape

counterpart. When evaluated against the AERONET AOD and AE observations at five sites over land, ORG_NSPH generates smaller RMSEs and mean biases, with greater improvement in AE (7.80% improvement in RMSE and 15.30% in MB) upon ORG_SPH. For the AOD spatial pattern, despite the great similarity shared by the two simulations, ORG_NSPH generally has higher AOD that extends farther west compared to ORG_SPH, leading to better agreement with the VIIRS observation. Enhanced dust optical properties and delayed sedimentation of non-spherical dust particles are responsible for the augmentation and westward extension of AOD in ORG_NSPH.

In addition to AOD analysis, we find that AE largely increases westward from the African coast in observation (up to ~40°W) and model, indicating a higher fraction of large particles near the coast and the gradually increasing dominance of small particles into the Atlantic Ocean. ORG_NSPH is more effective in long-range dust transport compared to ORG_SPH, as seen by lower AE values spreading farther west. The reduction of AE past 40°W in observation may be ascribed to marine aerosols, which are not included in our WRF-Dust model. Over the dusty (AOD > 0.25) regions in the model simulations, ORG_NSPH exhibits both smaller biases and RMSEs. Thus, non-spherical particle shape is crucial in dust simulation in which it enhances dust optical properties and improves dust long-range transport through non-spherical particles' enlarged cross section area and reduced particle sedimentation.

Building on the understanding of the dust particle shape effect, we incorporate GLO and LOC size distributions to examine any further improvement in AOD and AE. GLO_GSFC shows the greatest increase in AOD in comparison with ORG_GSFC (the same as ORG_NSPH in model configuration), followed by LOC_GSFC and LOC_FLG. The drastic amplification of modeled AOD in GLO_GSFC leads to overestimation, reflected by its high RMSE in AOD when evaluated against AERONET. The evaluation against AERONET AE reveals that LOC_FLG can produce the lowest AE values among all the experiments, best aligning with observations. The improvement in modeled AE demonstrates the importance of accounting proper emitted dust size distribution and radiation scheme in modeled particle size representation.

Despite sharing a similar AOD spatial pattern, the highest AOD magnitude throughout the domain can be seen in GLO_GSFC, while LOC_GSFC and LOC_FLG show similar degree of enhancement in AOD compared to ORG_GSFC. The enhancement in modeled AOD allows LOC_GSFC and LOC_FLG to capture the VIIRS observed AOD over the Algeria source region. However, all the simulations encounter the issues of AOD overestimation at the coast and underestimation at the inland source regions (e.g., Chad). While coastal Africa is subject to various factors such as marine aerosols and land and sea breezes, the inland dust hotspots are under the influence of local convective systems (i.e., haboobs) that pose further difficulty in dust simulation. Some potential solutions would be to incorporate soil erodibility in the WRF-Dust model for more accurate model dust emissions and to increase model resolution in an attempt to resolve local convection. As for modeled AE over ocean, LOC_FLG best replicates the VIIRS observed AE and has the greatest extent of low AEs into the central and western Atlantic. On average, LOC_FLG shows a 46% decrease in simulated AE compared to ORG_GSFC.

In the AE analysis over both land and ocean, contrary to LOC_FLG and GLO_GSFC, which improve considerably over ORG_GSFC, LOC_GSFC is comparable to or even slightly worse than ORG_GSFC. Several major factors in the LOC_GSFC setting are responsible for its less accurate AE representation: 1) the current WRF-Dust model size bins cover only up to 10 μm, meaning that the model is missing a substantial fraction of 10-20 μm coarse dust in the LOC distribution; 2) in the limited model size bin range, LOC favors bin 1 (i.e., the smallest bin) most strongly compared to ORG and GLO; smaller dust particles in the air contribute to higher AE values; and 3) the AOD values in different spectral bands captured by the GSFC radiation scheme can cause undesirably high AE values; since AE is in fact a relation of AODs at two separate wavelengths, the differences in radiation schemes' spectral bands and optical properties can cause discrepancies in the AE values computed. The simulation results of LOC_FLG testify that the different optical properties in the FLG scheme can indeed cause distinct simulated AEs (much lower than AEs in LOC_GSFC). On the other hand, GLO_GSFC, due to its high weightings on bins 2-4, can also generate relatively low AEs. Due to the nature of the GLO distribution, the combination of GLO_FLG would produce AEs that are unrealistically low AEs. Thus, GLO_FLG is excluded in our analysis.

The evaluation of modeled aerosol backscatter profiles against the CALIOP observations provides an important insight into the model's ability to simulate the vertical distribution of dust, which can influence dust-radiation and dust-cloud interactions. Near the surface (0-1 km), all the simulations show substantial deviation from the observation. From 2 to 4 km, LOC_FLG has the greatest alignment with the observed profile. However, LOC_FLG consistently underestimates the observed backscatter partially due to the reduction of the dimensional constant C (halved) when lowering the overshooting modeled AOD associated with the modified optical coefficients in the FLG scheme. On the contrary, GLO_GSFC displays uniform overestimation from 1.5 to 5 km. Across all the simulations, model errors decrease with height. Assimilating observed aerosol backscatter data may be the key to cope with the low-level underestimation of backscatter.

The best model configuration, LOC_FLG, is applied in the study on Hurricane Earl. In the AOD evaluation against MODIS observations, LOC_FLG replicates AOD magnitude slightly better than ORG_GSFC in particular at the western coast and north of the storm, although neither simulation can adequately transport dust to the storm region. With the improvement in AOD at the African coast and over the storm region, the modeled temperatures at 750- and 850-hPa pressure levels over those regions are enhanced in LOC_FLG compared to ORG_GSFC. We also found severe cold bias over land in ORG_GSFC, which was attributed to the optical properties in the GSFC scheme. Unlike temperature, there is minimal dust-induced wind improvement, as dust does not directly influence winds but via thermal wind relation. The simulated storm tracks for ORG_GSFC and LOC_FLG are nearly indistinguishable, and both deviate from the observed track from 1200 UTC 27 August 2010. However, LOC_FLG slightly increased the storm intensity, as seen from the lower minimum sea level pressure (~4 hPa lower) and higher maximum 10-m wind speed (~3 m/s higher) compared to ORG_GSFC after 0000 UTC 27 August, although the differences might not be significant. Our WRF-Dust model is still inadequate in reproducing the observed track and the storm's rapid intensification. Further dust improvement, resolution increase, and, potentially, data assimilation are necessary to reproduce the hurricane's development and environment.

The results of this study demonstrate that dust shape and emitted dust size distribution play a crucial role in dust modeling by reducing dust sedimentation, augmenting dust optical properties, and enhancing

dust long-range transport. For our region of interest, the emitted dust size distribution based on averaged local site measurements combined with the FLG radiation scheme and non-spherical adjustment (i.e., LOC_FLG) produced the most realistic dust simulation. Yet, there exist several limitations in our model. Our current WRF-Dust model is insufficient at wholly incorporating the observationally-constrained dust distribution from Adebiyi & Kok (2020). The largest size bin contains a median diameter of 8 μm, whereas the LOC and GLO distributions are computed up to 20 μm. This limitation poses a major drawback in model simulations, as a substantial fraction of coarse particles is concentrated beyond 10 μm in both distributions. Neglecting this portion could result in less accurate dust simulation, in particular in modeled dust-radiative effect and AE. Resolving this issue requires the model to encompass a greater size range of dust particles. Under these circumstances, we will extend our WRF-Dust model size coverage to 20 μm. Moreover, in the model evaluation against VIIRS observations, we realized that much of the discrepancy in AOD and AE between the model and observations lies in the contribution of marine aerosols, which are intrinsically absent in our WRF-Dust model. Missing marine aerosols in the model may result in underestimation of AOD and overestimation of AE over the ocean, especially farther away from source regions. Also, marine aerosols are highly involved in weather systems over the ocean, such as tropical cyclones. Thus, including marine aerosols will be a key task in our upcoming studies. Last but not least, a critical limitation is the difference in computation of optical properties in the two radiation schemes. For the FLG scheme, we employ a lookup table of tri-axial dust optical properties computed based on Meng et al. (2010), whereas the optical properties associated with the GSFC scheme are computed using Equation (3). This may introduce unnecessary discrepancies and lead to unfair comparison between experiments run with different schemes. Thus, formulating a lookup table for the GSFC scheme based on the same methodology and incorporating the modified optical coefficients into the GSFC experiments will be important future work.

References

Adebiyi, A. A., & Kok, J. F. (2020). Climate models miss most of the coarse dust in the atmosphere. *Science Advances*. https://doi.org/10.1126/sciadv.aaz9507

Adebiyi, A. A., Kok, J. F., Wang, Y., Ito, A., Ridley, D. A., Nabat, P., & Zhao, C. (2020). Dust Constraints from joint Observational-Modelling-experiMental analysis (DustCOMM): Comparison with measurements and model simulations. *Atmospheric Chemistry and Physics*. https://doi.org/10.5194/acp-20-829-2020

Ångström, A. (1929). On the Atmospheric Transmission of Sun Radiation and on Dust in the Air. *Geografiska Annaler*. https://doi.org/10.1080/20014422.1929.11880498

Ansmann, A., Rittmeister, F., Engelmann, R., Basart, S., Jorba, O., Spyrou, C., Remy, S., Skupin, A., Baars, H., Seifert, P., Senf, F., & Kanitz, T. (2017). Profiling of Saharan dust from the Caribbean to western Africa - Part 2: Shipborne lidar measurements versus forecasts. *Atmospheric Chemistry and Physics*, *17*(24), 14987–15006. https://doi.org/10.5194/acp-17-14987-2017

Arnalds, O., Gisladottir, F. O., & Sigurjonsson, H. (2001). Sandy deserts of Iceland: An overview. *Journal of Arid Environments*. https://doi.org/10.1006/jare.2000.0680

Bagheri, G., & Bonadonna, C. (2016). On the drag of freely falling non-spherical particles. *Powder Technology*. https://doi.org/10.1016/j.powtec.2016.06.015

Bercos-Hickey, E., Nathan, T. R., & Chen, S.-H. (2020). On the relationship between the African easterly jet, Saharan mineral dust aerosols, and west African precipitation. *Journal of Climate*. https://doi.org/10.1175/JCLI-D-18-0661.1

Berger, H., Forsythe, M., Eyre, J., & Healy, S. (2004). A superobbing scheme for atmospheric motion vectors. *Conference on Satellite Meteorology and Oceanography*.

Bi, L., Yang, P., Kattawar, G. W., & Kahn, R. (2009). Single-scattering properties of triaxial ellipsoidal particles for a size parameter range from the Rayleigh to geometric-optics regimes. *Applied Optics*, *48*(1), 114–126. https://doi.org/10.1364/AO.48.000114

Bi, L., Yang, P., Kattawar, G. W., & Kahn, R. (2010). Modeling optical properties of mineral aerosol particles by using nonsymmetric hexahedra. *Applied Optics*, *49*(3). https://doi.org/10.1364/AO.49.000334

Burnett, R. T., Arden Pope, C., Ezzati, M., Olives, C., Lim, S. S., Mehta, S., Shin, H. H., Singh, G., Hubbell, B., Brauer, M., Ross Anderson, H., Smith, K. R., Balmes, J. R., Bruce, N. G., Kan, H., Laden, F., Prüss-Ustün, A., Turner, M. C., Gapstur, S. M., … Cohen, A. (2014). An integrated risk function for estimating the global burden of disease attributable to ambient fine particulate matter exposure. *Environmental Health Perspectives*. https://doi.org/10.1289/ehp.1307049

Cangialosi, J. P. (2011). *Tropical Cyclone Report: Hurricane Earl* (AL072010). National Hurricane Center. https://www.nhc.noaa.gov/data/tcr/AL072010_Earl.pdf

Carlson, T. N., & Benjamin, S. G. (1980). Radiative heating rates for Saharan dust. *Journal of the Atmospheric Sciences*, *37*(1). https://doi.org/10.1175/1520-0469(1980)037<0193:RHRFSD>2.0.CO;2

Chen, G., Wang, W. C., & Chen, J. P. (2015). Aerosol-stratocumulus-radiation interactions over the southeast Pacific. *Journal of the Atmospheric Sciences*, *72*(7). https://doi.org/10.1175/JAS-D-14-0319.1

Chen, S.-H., Liu, Y. C., Nathan, T. R., Davis, C., Torn, R., Sowa, N., Cheng, C. T., & Chen, J. P. (2015). Modeling the effects of dust-radiative forcing on the movement of Hurricane Helene (2006). *Quarterly Journal of the Royal Meteorological Society*. https://doi.org/10.1002/qj.2542

Chen, S.-H., Wang, S. H., & Waylonis, M. (2010). Modification of Saharan air layer and environmental shear over the eastern Atlantic Ocean by dust-radiation effects. *Journal of Geophysical Research Atmospheres*. https://doi.org/10.1029/2010JD014158

Cheng, C. T., Wang, W. C., & Chen, J. P. (2010). Simulation of the effects of increasing cloud condensation nuclei on mixed-phase clouds and precipitation of a front system. *Atmospheric Research*. https://doi.org/10.1016/j.atmosres.2010.02.005

Choi, Y., Chen, S.-H., Huang, C.-C., Earl, K., Chen, C. Y., Schwartz, C. S., & Matsui, T. (2020). Evaluating the Impact of Assimilating Aerosol Optical Depth Observations on Dust Forecasts Over North Africa and the East Atlantic Using Different Data Assimilation Methods. *Journal of Advances in Modeling Earth Systems*, *12*(4), 1–30. https://doi.org/10.1029/2019MS001890

Chou, C., Formenti, P., Maille, M., Ausset, P., Helas, G., Harrison, M., & Osborne, S. (2008). Size distribution, shape, and composition of mineral dust aerosols collected during the African Monsoon Multidisciplinary Analysis Special Observation Period 0: Dust and Biomass-Burning Experiment field campaign in Niger, January 2006. *Journal of Geophysical Research Atmospheres*. https://doi.org/10.1029/2008JD009897

Chou, M.-D., & Suarez, M. J. (1994). An efficient thermal infrared radiation parameterization for use in general circulation models. *Nasa Tech. Memo*.

Chou, M.-D., & Suarez, M. J. (1999). A solar radiation parameterization (CLIRAD-SW) for atmospheric studies. *NASA Tech. Memo*.

Chou, M.-D., Suarez, M. J., Liang, X.-Z., & Yan, M. M.-H. (2001). A Thermal Infrared Radiation Parameterization for Atmospheric Studies. *NASA Technical Report*.

Cuevas, E., Camino, C., Benedetti, A., Basart, S., Terradellas, E., Baldasano, J. M., Morcrette, J. J., Marticorena, B., Goloub, P., Mortier, A., Berjón, A., Hernández, Y., Gil-Ojeda, M., & Schulz, M. (2015). The MACC-II 2007-2008 reanalysis: atmospheric dust evaluation and characterization over northern Africa and the Middle East. *Atmospheric Chemistry and Physics*, *15*(8). https://doi.org/10.5194/acp-15-3991-2015

DeMott, P. J., Sassen, K., Poellot, M. R., Baumgardner, D., Rogers, D. C., Brooks, S. D., Prenni, A. J., & Kreidenweis, S. M. (2003). African dust aerosols as atmospheric ice nuclei. *Geophysical Research Letters*. https://doi.org/10.1029/2003GL017410

Dubovik, O., Holben, B. N., Lapyonok, T., Sinyuk, A., Mishchenko, M. I., Yang, P., & Slutsker, I. (2002). Non-spherical aerosol retrieval method employing light scattering by spheroids. *Geophysical Research Letters*. https://doi.org/10.1029/2001gl014506

Dubovik, O., Sinyuk, A., Lapyonok, T., Holben, B. N., Mishchenko, M., Yang, P., Eck, T. F., Volten, H., Muñoz, O., Veihelmann, B., van der Zande, W. J., Leon, J. F., Sorokin, M., & Slutsker, I. (2006). Application of spheroid models to account for aerosol particle nonsphericity in remote sensing of desert dust. *Journal of Geophysical Research Atmospheres*, *111*(11). https://doi.org/10.1029/2005JD006619

Engelstaedter, S., & Washington, R. (2007). Atmospheric controls on the annual cycle of North African dust. *Journal of Geophysical Research Atmospheres*. https://doi.org/10.1029/2006JD007195

Fan, J., Wang, Y., Rosenfeld, D., & Liu, X. (2016). Review of aerosol-cloud interactions: Mechanisms, significance, and challenges. In *Journal of the Atmospheric Sciences*. https://doi.org/10.1175/JAS-D-16-0037.1

Fu, Q., & Liou, K. N. (1992). On the correlated k-distribution method for radiative transfer in nonhomogeneous atmospheres. *Journal of the Atmospheric Sciences*. https://doi.org/10.1175/1520-0469(1992)049<2139:otcdmf>2.0.co;2

García-Pando, C. P., Stanton, M. C., Diggle, P. J., Trzaska, S., Miller, R. L., Perlwitz, J. P., Baldasano, J. M., Cuevas, E., Ceccato, P., Yaka, P., & Thomson, M. C. (2014). Soil dust aerosols and wind as predictors of seasonal meningitis incidence in niger. *Environmental Health Perspectives*. https://doi.org/10.1289/ehp.1306640

Giles, D. M., Sinyuk, A., Sorokin, M. G., Schafer, J. S., Smirnov, A., Slutsker, I., Eck, T. F., Holben, B. N., Lewis, J. R., Campbell, J. R., Welton, E. J., Korkin, S. V., & Lyapustin, A. I. (2019). Advancements in the Aerosol Robotic Network (AERONET) Version 3 database - Automated near-real-time quality control algorithm with improved cloud screening for Sun photometer aerosol optical depth (AOD) measurements. *Atmospheric Measurement Techniques*. https://doi.org/10.5194/amt-12-169-2019

Ginoux, P. (2003). Effects of nonsphericity on mineral dust modeling. *Journal of Geophysical Research: Atmospheres*. https://doi.org/10.1029/2002jd002516

Gu, Y., Liou, K. N., Ou, S. C., & Fovell, R. (2011). Cirrus cloud simulations using WRF with improved radiation parameterization and increased vertical resolution. *Journal of Geophysical Research Atmospheres*. https://doi.org/10.1029/2010JD014574

Hersbach, H., Bell, B., Berrisford, P., Hirahara, S., Horányi, A., Muñoz-Sabater, J., Nicolas, J., Peubey, C., Radu, R., Schepers, D., Simmons, A., Soci, C., Abdalla, S., Abellan, X., Balsamo, G., Bechtold, P., Biavati, G., Bidlot, J., Bonavita, M., … Thépaut, J. N. (2020). The ERA5 global reanalysis. *Quarterly Journal of the Royal Meteorological Society*. https://doi.org/10.1002/qj.3803

Hess, M., Koepke, P., & Schult, I. (1998). Optical Properties of Aerosols and Clouds: The Software Package OPAC. *Bulletin of the American Meteorological Society*. https://doi.org/10.1175/1520-0477(1998)079<0831:OPOAAC>2.0.CO;2

Hong, S. Y., & Pan, H. L. (1996). Nonlocal boundary layer vertical diffusion in a medium-range forecast model. *Monthly Weather Review*. https://doi.org/10.1175/1520-0493(1996)124<2322:NBLVDI>2.0.CO;2

Hoshyaripour, G. A., Bachmann, V., Förstner, J., Steiner, A., Vogel, H., Wagner, F., Walter, C., & Vogel, B. (2019). Effects of Particle Nonsphericity on Dust Optical Properties in a Forecast System: Implications for Model-Observation Comparison. *Journal of Geophysical Research: Atmospheres*. https://doi.org/10.1029/2018JD030228

Huang, C.-C., Chen, S.-H., Lin, Y. C., Earl, K., Matsui, T., Lee, H. H., Tsai, I. C., Chen, J. P., & Cheng, C. T. (2019). Impacts of dust-radiation versus dust-cloud interactions on the development of a modeled mesoscale convective system over North Africa. *Monthly Weather Review*. https://doi.org/10.1175/MWR-D-18-0459.1

Huang, Y., Kok, J. F., Kandler, K., Lindqvist, H., Nousiainen, T., Sakai, T., Adebiyi, A., & Jokinen, O. (2020). Climate Models and Remote Sensing Retrievals Neglect Substantial Desert Dust Asphericity. *Geophysical Research Letters*. https://doi.org/10.1029/2019GL086592

Huneeus, N., Schulz, M., Balkanski, Y., Griesfeller, J., Prospero, J., Kinne, S., Bauer, S., Boucher, O., Chin, M., Dentener, F., Diehl, T., Easter, R., Fillmore, D., Ghan, S., Ginoux, P., Grini, A., Horowitz, L., Koch, D., Krol, M. C., … Zender, C. S. (2011). Global dust model intercomparison in AeroCom phase i. *Atmospheric Chemistry and Physics*, *11*(15). https://doi.org/10.5194/acp-11-7781-2011

Jickells, T. D., An, Z. S., Andersen, K. K., Baker, A. R., Bergametti, C., Brooks, N., Cao, J. J., Boyd, P. W., Duce, R. A., Hunter, K. A., Kawahata, H., Kubilay, N., LaRoche, J., Liss, P. S., Mahowald, N., Prospero, J. M., Ridgwell, A. J., Tegen, I., & Torres, R. (2005). Global iron connections between desert dust, ocean biogeochemistry, and climate. In *Science*. https://doi.org/10.1126/science.1105959

Jiménez, P. A., Dudhia, J., González-Rouco, J. F., Navarro, J., Montávez, J. P., & García-Bustamante, E. (2012). A revised scheme for the WRF surface layer formulation. *Monthly Weather Review*. https://doi.org/10.1175/MWR-D-11-00056.1

Kalashnikova, O. V., & Sokolik, I. N. (2004). Modeling the radiative properties of nonspherical soil-derived mineral aerosols. *Journal of Quantitative Spectroscopy and Radiative Transfer*. https://doi.org/10.1016/j.jqsrt.2003.12.026

Kandler, K., Benker, N., Bundke, U., Cuevas, E., Ebert, M., Knippertz, P., Rodríguez, S., Schütz, L., & Weinbruch, S. (2007). Chemical composition and complex refractive index of Saharan Mineral Dust at Izaña, Tenerife (Spain) derived by electron microscopy. *Atmospheric Environment*. https://doi.org/10.1016/j.atmosenv.2007.06.047

Kim, D., Chin, M., Yu, H., Diehl, T., Tan, Q., Kahn, R. A., Tsigaridis, K., Bauer, S. E., Takemura, T., Pozzoli, L., Bellouin, N., Schulz, M., Peyridieu, S., Chédin, A., & Koffi, B. (2014). Sources, sinks, and transatlantic transport of North African dust aerosol: A multimodel analysis and comparison with remote sensing data. *Journal of Geophysical Research*. https://doi.org/10.1002/2013JD021099

Kinne, S., Schulz, M., Textor, C., Guibert, S., Balkanski, Y., Bauer, S. E., Berntsen, T., Berglen, T. F., Boucher, O., Chin, M., Collins, W., Dentener, F., Diehl, T., Easter, R., Feichter, J., Fillmore, D.,

Ghan, S., Ginoux, P., Gong, S., … Tie, X. (2006). An AeroCom initial assessment - Optical properties in aerosol component modules of global models. *Atmospheric Chemistry and Physics*, *6*(7). https://doi.org/10.5194/acp-6-1815-2006

Klaver, A., Formenti, P., Caquineau, S., Chevaillier, S., Ausset, P., Calzolai, G., Osborne, S., Johnson, B., Harrison, M., & Dubovik, O. (2011). Physico-chemical and optical properties of sahelian and saharan mineral dust: In situ measurements during the gerbils campaign. *Quarterly Journal of the Royal Meteorological Society*. https://doi.org/10.1002/qj.889

Knippertz, P., & Todd, M. C. (2010). The central west Saharan dust hot spot and its relation to African easterly waves and extratropical disturbances. *Journal of Geophysical Research Atmospheres*, *115*(12). https://doi.org/10.1029/2009JD012819

Koepke, P., Gasteiger, J., & Hess, M. (2015). Technical Note: Optical properties of desert aerosol with non-spherical mineral particles: Data incorporated to OPAC. *Atmospheric Chemistry and Physics*. https://doi.org/10.5194/acp-15-5947-2015

Kok, J. F. (2011). A scaling theory for the size distribution of emitted dust aerosols suggests climate models underestimate the size of the global dust cycle. *Proceedings of the National Academy of Sciences of the United States of America*. https://doi.org/10.1073/pnas.1014798108

Kok, J. F., Ridley, D. A., Zhou, Q., Miller, R. L., Zhao, C., Heald, C. L., Ward, D. S., Albani, S., & Haustein, K. (2017). Smaller desert dust cooling effect estimated from analysis of dust size and abundance. *Nature Geoscience*. https://doi.org/10.1038/ngeo2912

Konare, A., Zakey, A. S., Solmon, F., Giorgi, F., Rauscher, S., Ibrah, S., & Bi, X. (2008). A regional climate modeling study of the effect of desert dust on the West African monsoon. *Journal of Geophysical Research Atmospheres*, *113*(12). https://doi.org/10.1029/2007JD009322

Laken, B. A., Parviainen, H., Pallé, E., & Shahbaz, T. (2014). Saharan mineral dust outbreaks observed over the North Atlantic island of La Palma in summertime between 1984 and 2012. *Quarterly Journal of the Royal Meteorological Society*, *140*(680). https://doi.org/10.1002/qj.2170

Lavaysse, C., Flamant, C., Janicot, S., Parker, D. J., Lafore, J. P., Sultan, B., & Pelon, J. (2009). Seasonal evolution of the West African heat low: A climatological perspective. *Climate Dynamics*. https://doi.org/10.1007/s00382-009-0553-4

Levy, R. C., Remer, L. A., Martins, J. V., Kaufman, Y. J., Plana-Fattori, A., Redemann, J., & Wenny, B. (2005). Evaluation of the MODIS aerosol retrievals over ocean and land during CLAMS. *Journal of the Atmospheric Sciences*. https://doi.org/10.1175/JAS3391.1

Li, S., Yu, C., Chen, L., Tao, J., Letu, H., Ge, W., Si, Y., & Liu, Y. (2016). Inter-comparison of model-simulated and satellite-retrieved componential aerosol optical depths in China. *Atmospheric Environment*, *141*. https://doi.org/10.1016/j.atmosenv.2016.06.075

Lieke, K., Kandler, K., Scheuvens, D., Emmel, C., Von Glahn, C., Petzold, A., Weinzierl, B., Veira, A., Ebert, M., Weinbruch, S., & Schütz, L. (2011). Particle chemical properties in the vertical column based on aircraft observations in the vicinity of Cape Verde Islands. *Tellus, Series B: Chemical and Physical Meteorology*. https://doi.org/10.1111/j.1600-0889.2011.00553.x

Ma, P. L., Zhang, K., Shi, J. J., Matsui, T., & Arking, A. (2012). Direct radiative effect of mineral dust on the development of African easterly waves in late summer, 2003-07. *Journal of Applied Meteorology and Climatology*, *51*(12). https://doi.org/10.1175/JAMC-D-11-0215.1

Matsui, T., Iguchi, T., Li, X., Han, M., Tao, W. K., Petersen, W., L'Ecuyer, T., Meneghini, R., Olson, W., Kummerow, C. D., Hou, A. Y., Schwaller, M. R., Stocker, E. F., & Kwiatkowski, J. (2013). GPM satellite simulator over ground validation sites. *Bulletin of the American Meteorological Society*. https://doi.org/10.1175/BAMS-D-12-00160.1

Matsui, T., Santanello, J., Shi, J. J., Tao, W. K., Wu, D., Peters-Lidard, C., Kemp, E., Chin, M., Starr, D., Sekiguchi, M., & Aires, F. (2014). Introducing multisensor satellite radiance-based evaluation for regional earth system modeling. *Journal of Geophysical Research*. https://doi.org/10.1002/2013JD021424

Meng, Z., Yang, P., Kattawar, G. W., Bi, L., Liou, K. N., & Laszlo, I. (2010). Single-scattering properties of tri-axial ellipsoidal mineral dust aerosols: A database for application to radiative transfer calculations. *Journal of Aerosol Science*. https://doi.org/10.1016/j.jaerosci.2010.02.008

Min, Q. L., Li, R., Lin, B., Joseph, E., Wang, S., Hu, Y., Morris, V., & Chang, F. (2009). Evidence of mineral dust altering cloud microphysics and precipitation. *Atmospheric Chemistry and Physics*, *9*(9). https://doi.org/10.5194/acp-9-3223-2009

Mishchenko, M. I., Travis, L. D., Kahn, R. A., & West, R. A. (1997). Modeling phase functions for dustlike tropospheric aerosols using a shape mixture of randomly oriented polydisperse spheroids. *Journal of Geophysical Research Atmospheres*, *102*(14). https://doi.org/10.1029/96jd02110

Morman, S. A., & Plumlee, G. S. (2013). The role of airborne mineral dusts in human disease. In *Aeolian Research*. https://doi.org/10.1016/j.aeolia.2012.12.001

Nathan, T. R., Grogan, D. F. P., & Chen, S.-H. (2017). Subcritical destabilization of African easterly waves by Saharan mineral dust. *Journal of the Atmospheric Sciences*, *74*(4). https://doi.org/10.1175/JAS-D-16-0247.1

Nathan, T. R., Grogan, D. F. P., & Chen, S.-H. (2019). Saharan dust transport during the incipient growth phase of African Easterly waves. *Geosciences (Switzerland)*, *9*(9). https://doi.org/10.3390/geosciences9090388

Nousiainen, T. (2009). Optical modeling of mineral dust particles: A review. In *Journal of Quantitative Spectroscopy and Radiative Transfer*. https://doi.org/10.1016/j.jqsrt.2009.03.002

O'Sullivan, D., Marenco, F., Ryder, C., Pradhan, Y., Kipling, Z., Johnson, B., Benedetti, A., Brooks, M., McGill, M., Yorks, J., & Selmer, P. (2020). Models transport Saharan dust too low in the atmosphere compared to observations. *Atmospheric Chemistry and Physics Discussions*. https://doi.org/10.5194/acp-2020-57

Pandolfi, M., Tobias, A., Alastuey, A., Sunyer, J., Schwartz, J., Lorente, J., Pey, J., & Querol, X. (2014). Effect of atmospheric mixing layer depth variations on urban air quality and daily mortality during Saharan dust outbreaks. *Science of the Total Environment*. https://doi.org/10.1016/j.scitotenv.2014.07.004

Penner, J. E., Zhang, S. Y., Chin, M., Chuang, C. C., Feichter, J., Feng, Y., Geogdzhayev, I. V., Ginoux, P., Herzog, M., Higurashi, A., Koch, D., Land, C., Lohmann, U., Mishchenko, M., Nakajima, T., Pitari, G., Soden, B., Tegen, I., & Stowe, L. (2002). A comparison of model- and satellite-derived aerosol optical depth and reflectivity. *Journal of the Atmospheric Sciences*, *59*(3). https://doi.org/10.1175/1520-0469(2002)059%3C0441%3AACOMAS%3E2.0.C

Pérez, C., Nickovic, S., Pejanovic, G., Baldasano, J. M., & Özsoy, E. (2006). Interactive dust-radiation modeling: A step to improve weather forecasts. *Journal of Geophysical Research Atmospheres*. https://doi.org/10.1029/2005JD006717

Prospero, J. M., Ginoux, P., Torres, O., Nicholson, S. E., & Gill, T. E. (2002). Environmental characterization of global sources of atmospheric soil dust identified with the Nimbus 7 Total Ozone Mapping Spectrometer (TOMS) absorbing aerosol product. *Reviews of Geophysics*. https://doi.org/10.1029/2000RG000095

Potenza, M. A. C., Albani, S., Delmonte, B., Villa, S., Sanvito, T., Paroli, B., Pullia, A., Baccolo, G., Mahowald, N., & Maggi, V. (2016). Shape and size constraints on dust optical properties from the Dome C ice core, Antarctica. *Scientific Reports*. https://doi.org/10.1038/srep28162

Reid, E. A., Reid, J. S., Meier, M. M., Dunlap, M. R., Cliff, S. S., Broumas, A., Perry, K., & Maring, H. (2003). Characterization of African dust transported to Puerto Rico by individual particle and size segregated bulk analysis. *Journal of Geophysical Research: Atmospheres*. https://doi.org/10.1029/2002jd002935

Ryder, C. L., Highwood, E. J., Walser, A., Seibert, P., Philipp, A., & Weinzierl, B. (2019). Coarse and giant particles are ubiquitous in Saharan dust export regions and are radiatively significant over the Sahara. *Atmospheric Chemistry and Physics*, *19*(24), 15353–15376. https://doi.org/10.5194/acp-19-15353-2019

Sayer, A. M., Hsu, N. C., Lee, J., Bettenhausen, C., Kim, W. V., & Smirnov, A. (2018). Satellite Ocean Aerosol Retrieval (SOAR) Algorithm Extension to S-NPP VIIRS as Part of the "Deep Blue" Aerosol Project. *Journal of Geophysical Research: Atmospheres*. https://doi.org/10.1002/2017JD027412

Shi, J. J., Matsui, T., Tao, W. K., Tan, Q., Peters-Lidard, C., Chin, M., Pickering, K., Guy, N., Lang, S., & Kemp, E. M. (2014). Implementation of an aerosol-cloud-microphysics-radiation coupling into the NASA unified WRF: Simulation results for the 6-7 August 2006 AMMA special observing period. *Quarterly Journal of the Royal Meteorological Society*. https://doi.org/10.1002/qj.2286

Skamarock WC, et al. (2008). A description of the advanced research WRF version 3, NCAR Tech. Note, NCAR/TN-468+STR. *Natl. Cent. for Atmos. Res. Boulder, Colorado*.

Slingo, A., Ackerman, T. P., Allan, R. P., Kassianov, E. I., McFarlane, S. A., Robinson, G. J., Barnard, J. C., Miller, M. A., Harries, J. E., Russell, J. E., & Dewitte, S. (2006). Observations of the impact of a major Saharan dust storm on the atmospheric radiation balance. *Geophysical Research Letters*. https://doi.org/10.1029/2006GL027869

Smirnov, A., Holben, B. N., Slutsker, I., Giles, D. M., McClain, C. R., Eck, T. F., Sakerin, S. M., Macke, A., Croot, P., Zibordi, G., Quinn, P. K., Sciare, J., Kinne, S., Harvcy, M., Smyth, T. J., Piketh, S., Zielinski, T., Proshutinsky, A., Goes, J. I., … Jourdin, F. (2009). Maritime Aerosol Network as a

component of Aerosol Robotic Network. *Journal of Geophysical Research Atmospheres*, *114*(6). https://doi.org/10.1029/2008JD011257

Smirnov, A., Holben, B. N., Giles, D. M., Slutsker, I., O'Neill, N. T., Eck, T. F., MacKe, A., Croot, P., Courcoux, Y., Sakerin, S. M., Smyth, T. J., Zielinski, T., Zibordi, G., Goes, J. I., Harvey, M. J., Quinn, P. K., Nelson, N. B., Radionov, V. F., Duarte, C. M., … Diehl, T. L. (2011). Maritime aerosol network as a component of AERONET - First results and comparison with global aerosol models and satellite retrievals. *Atmospheric Measurement Techniques*, *4*(3). https://doi.org/10.5194/amt-4-583-2011

Soni, K., Singh, S., Bano, T., Tanwar, R. S., & Nath, S. (2011). Wavelength dependence of the aerosol Angstrom exponent and its implications over Delhi, India. *Aerosol Science and Technology*. https://doi.org/10.1080/02786826.2011.601774

Stauffer, D. R., & Seaman, N. L. (1990). Use of four-dimensional data assimilation in a limited-area mesoscale model. Part I: experiments with synoptic-scale data. *Monthly Weather Review*, *118*(6). https://doi.org/10.1175/1520-0493(1990)118<1250:UOFDDA>2.0.CO;2

Tegen, I., & Fung, I. (1994). Modeling of mineral dust in the atmosphere: sources, transport, and optical thickness. *Journal of Geophysical Research*. https://doi.org/10.1029/94jd01928

Tegen, I. (2003). Modeling the mineral dust aerosol cycle in the climate system. *Quaternary Science Reviews*. https://doi.org/10.1016/S0277-3791(03)00163-X

Tewari, M., Chen, F., Wang, W., Dudhia, J., LeMone, M. A., Mitchell, K., Ek, M., Gayno, G., Wegiel, J., & Cuenca, R. H. (2004). Implementation and verification of the unified noah land surface model in the WRF model. *Bulletin of the American Meteorological Society*.

Toth, T. D., Campbell, J. R., Reid, J. S., Tackett, J. L., Vaughan, M. A., Zhang, J., & Marquis, J. W. (2018). Minimum aerosol layer detection sensitivities and their subsequent impacts on aerosol optical thickness retrievals in CALIPSO level 2 data products. *Atmospheric Measurement Techniques*, *11*(1). https://doi.org/10.5194/amt-11-499-2018

Wang, M., Su, J., Li, X., Wang, C., & Ge, J. (2019). Parameterization of the single-scattering properties of dust aerosols in radiative flux calculations. *Atmosphere*. https://doi.org/10.3390/ATMOS10120728

Wang, R., Balkanski, Y., Bopp, L., Aumont, O., Boucher, O., Ciais, P., Gehlen, M., Peñuelas, J., Ethé, C., Hauglustaine, D., Li, B., Liu, J., Zhou, F., & Tao, S. (2015). Influence of anthropogenic aerosol deposition on the relationship between oceanic productivity and warming. *Geophysical Research Letters*. https://doi.org/10.1002/2015GL066753

Winker, D. M., Hostetler, C. A., & Hunt, W. H. (2003). Cloud-Aerosol LIdar with Orthogonal Polarization (CALIOP). *International Geoscience and Remote Sensing Symposium (IGARSS)*. https://doi.org/10.1109/igarss.2003.1294160

Wong, S., Dessler, A. E., Mahowald, N. M., Yang, P., & Feng, Q. (2009). Maintenance of lower tropospheric temperature inversion in the Saharan air layer by dust and dry anomaly. *Journal of Climate*, *22*(19). https://doi.org/10.1175/2009JCLI2847.1

Yang, W., Marshak, A., Kostinski, A. B., & Várnai, T. (2013). Shape-induced gravitational sorting of Saharan dust during transatlantic voyage: Evidence from CALIOP lidar depolarization measurements. *Geophysical Research Letters*. https://doi.org/10.1002/grl.50603

Yu, H., Chin, M., Yuan, T., Bian, H., Remer, L. A., Prospero, J. M., Omar, A., Winker, D., Yang, Y., Zhang, Y., Zhang, Z., & Zhao, C. (2015). The fertilizing role of African dust in the Amazon rainforest: A first multiyear assessment based on data from Cloud-Aerosol Lidar and Infrared Pathfinder Satellite Observations. *Geophysical Research Letters*. https://doi.org/10.1002/2015GL063040

Zhang, C., & Wang, Y. (2017). Projected future changes of tropical cyclone activity over the Western North and South Pacific in a 20-km-Mesh regional climate model. *Journal of Climate*, *30*(15). https://doi.org/10.1175/JCLI-D-16-0597.1

Zhu, A., Ramanathan, V., Li, F., & Kim, D. (2007). Dust plumes over the Pacific, Indian, and Atlantic oceans: Climatology and radiative impact. *Journal of Geophysical Research Atmospheres*, *112*(16). https://doi.org/10.1029/2007JD008427